國立陽明大學
神經科學研究所
博士論文

中央外側杏仁核的連結特異性與突觸多樣性

侯文賢 撰

105
08

中央外側杏仁核的連結特異性與突觸多樣性

Wiring specificity and synaptic diversity in the mouse lateral central amygdala

研究生：侯文賢（Wen-Hsien Hou）

指導教授：連正章 博士 (Cheng-Chang Lien, M.D., Ph.D.)

國立陽明大學

神經科學研究所

博 士 論 文

Institute of Neuroscience

National Yang-Ming University

Doctoral Dissertation

中華民國一〇五年八月

August, 2016

誌謝

首先要感謝連正章老師讓我有機會進入這個實驗室學習神經電生理，讓我有機會接觸神經科學，啟發我對於研究的興趣與保持做研究的熱情。在我的研究有初步結果時，是您鼓勵我申請博士班，並教導我如何成為一個好的科學家。不論是在實驗設計、資料分析與統計，甚至是圖的製作、文章修改方面都替我打下基礎。在我的計畫遇到瓶頸時，您協助我解決問題，並鼓勵我不要放棄。也特別感謝您給我多次參與國際研討會或是出國進修的機會，讓我能在學習新的技術，同時也拓展自己的視野，體認到自己的不足加以補強。

五年中大部分的時間都待在實驗室中，跟各位實驗室成員相處的時光也是我最珍貴的回憶。在我剛進來實驗室的時候，翁儒韻、劉于超、江柏翰、李政達、吳僕射、簡大鈞、黃昱尹、許燦庭、詹筑方、林晏竹、郭寧、郭子維、王思懿、許志緯這些實驗室的學長姊提供了一個良好的討論環境，並教會我電生理的基本觀念與技術。感謝 Dr. 翁與劉于超對於我的實驗方向提供許多建議。感謝達叔與僕射成為我在實驗室中的好夥伴，陪我奮戰到深夜。感謝陳建錞與陳亭伃這兩位實驗室的同儕陪我一起度過修神總，報 seminar 的苦日子。感謝顏廷耘與陳玠汝這兩位開心果帶給實驗室跟我許多歡笑。感謝高敏華、林昱伶、王凱誼、紀廷璇、衛昱廷、黃慧怡、陳勤霖、Amy、Frank、陳彥竹這些學弟妹幫我分擔許多實驗室的事務，並在我低潮時給我許多精神上的鼓舞。

由於專注在實驗中，常常會忽略家人。感謝爸爸媽媽無條件地提供我一切生活上所需要的幫助且不用擔心經濟問題，包容我的任性，也不抱怨我不常回家見您們。謝謝其他家人身體狀況一切健康，讓我能繼續專心在研究生活中。謝謝妹妹願意聽我分享生活中或研究時遇到的困難。謝謝王慕儀在四年半與 paper 最後要 revision 研究生日子裡，能包容我不正常的作息並聽我抱怨生活中的不順遂。

最後感謝所有在生活中所接觸過以及給予過我任何幫助的人，也感謝翻開這本書的任何人。

侯文賢

中華民國一〇五年八月十六日

中文摘要

中央杏仁核是一個絕大多數為釋放γ-氨基丁酸的神經細胞組成的皮質下結構，經由對位於下視丘與腦幹下游目標的投射控制恐懼行為的表現。中央杏仁核由外側與內側細分區構成。中央杏仁核外側區強力地控制傳遞到杏仁核主要輸出站之中央杏仁核內側區的訊息，但此區域中的局部迴路的功能性組成所知甚少。

使用集群分析，我們在小鼠杏仁核切片中辨識出兩類電生理特性相異的中央杏仁核外側區神經細胞，早期動作電位與晚期動作電位神經細胞。這兩群細胞表現不同的自身突觸傳導。相對於晚期動作電位細胞，早期動作電位細胞有強大與壓抑型的自身突觸，這增強了動作電位時間點的準確度。

藉由多重膜電位箝制紀錄，我發現中央杏仁核外側區神經細胞製造化學性突觸，但並沒有電性突觸。單一連結的分析展示在早期動作電位細胞的輸出突觸的第一型大麻素受體調控抑制，但並未發生在晚期動作電位細胞的輸出突觸。更加有趣的是，早期動作電位細胞→晚期動作電位細胞或晚期動作電位細胞→早期動作電位細胞的突觸功效約為晚期動作電位細胞→晚期動作電位細胞或早期動作電位細胞→早期動作電位細胞的兩倍。當用 20 赫茲測試時，不同種類神經細胞間的突觸，而非同種類神經細胞間的突觸，表現明顯的壓抑型且能較強力地雕塑

突觸後神經細胞的活性。不僅如此，不同種類神經細胞形成突觸的連結率較高。

總體來說，這篇研究說明了在中央杏仁核外側區中早期動作電位與晚期動作電位神經細胞代表兩群功能性相異的細胞種類以及突觸前與突觸後神經細胞間的互動決定了神經細胞間的突觸性能。

Abstract

The central amygdala (CeA) nucleus, a subcortical structure composed of mostly γ-aminobutyric acid-releasing (GABAergic) neurons, controls fear expression via projections to downstream targets in the hypothalamus and brainstem. The CeA consists of the lateral (CeL) and medial (CeM) subdivisions. The CeL strongly gates information transfer to the CeM, the main output station of the amygdala, but little is known about the functional organization of local circuits in this region.

Using cluster analysis, I identified two major electrophysiologically distinct CeL neuron classes in mouse amygdala slices, the early-spiking (ES) and late-spiking (LS) neurons. These two classes displayed distinct autaptic transmission. Compared with LS neurons, ES neurons had strong and depressing autapses, which enhanced spike-timing precision.

With multiple patch-clamp recordings, I found that CeL neurons made chemical, but not electrical, synapses. Analysis of individual connections revealed cannabinoid type 1 receptor-mediated suppression of the ES, but not of the LS cell output synapse. More interestingly, the efficacy of the ES→LS or LS→ES synapse was

approximately 2-fold greater than that of the LS→LS or ES→ES synapse. When tested at 20 Hz, synapses between different neurons, but not within the same class, were markedly depressing and were more powerful to sculpt activity of postsynaptic neurons. Moreover, neurons of different classes also form synapses with higher degree of connectivity.

Taken together, this study illustrates that ES and LS neurons represent two functionally distinct cell classes in the CeL and interactions between pre- and postsynaptic neurons dictate synaptic properties between neurons.

Table of contents

Abbreviations

2-AG, arachidonoyl glycerol
4-AP, 4-amino-pyridine
AEA, N-arachidonoylethanolamine
adBNST, anterodorsal BNST
α-DTX, α-dendrotoxin
aIPSC, autaptic inhibitory postsynaptic current
aIPSG, autaptic conductance
aIPSP, autaptic inhibitory postsynaptic potential
AP, Action potential
BA, basal nucleus of BLA
BLA, basolateral amygdala complex
CB_1R, cannabinoid receptor type 1
CB_2R, cannabinoid receptor type 2
CCK, cholecystokinin
CeA, central amygdala
CeL, lateral subdivision of CeA
CeM, medial subdivision of CeA
CS, conditioned stimulus
CR, conditioned fear responses
DSE, depolarization-induced suppression of excitation
DSI, depolarization-induced suppression of inhibition
eCB, endocannabinoid
E_{GABA}, equilibrium potentials for $GABA_A$ receptor-mediated currents
ES, early-spiking
FITC, fluorescein isothiocyanate
GABAergic, γ-aminobutyric acid-releasing
GPCR, G-protein coupled receptor
HPC, hippocampus
Ic, current-clamp
ICM, intercalated cell mass
ICM_L, lateral ICM
ICM_M, medial ICM
ICM_{MD}, medial dorsal ICM

ICM_{MV}, medial ventral ICM
I_D, D-type K^+ current
lPB, lateral parabrachial nucleus
LTB, low-threshold bursting
KO, knockout
Kv1, voltage gated K^+ channel type 1
LS, late-spiking
NAc, nucleus accumbens
PAG, periaqueductal gray
PBS, phosphate-buffered solution
PKC-δ, protein kinase C-δ
PFCs, prefrontal cortices
RMP, resting membrane potential (RMP)
R_N, input resistance
RS, regular spiking
r_s, Spearman rank correlation coefficient
SOM, somatostatin
STP, short-term plasticity
US, unconditioned stimulus
uIPSC, unitary inhibitory postsynaptic current
Vc, voltage-clamp
VGCC, voltage-dependent calcium channel
vHPC, ventral HPC
V_m, membrane potential
$\tau_{m,}$ membrane time constant

Chapter 1 | Background and Specific Aims

1. The network and function of amygdala

1a. The amygdala

The amygdala, named as an almond-like structure, is located in the medial temporal lobe region that plays a central role in many kinds of emotional behaviors such as Pavlovian conditioned fear or the anxiety-like behaviors (Ledoux, 2007; Ledoux, 2012). The amygdala is comprised of multiple interconnected nuclei where neurons form both inter- and intra-nucleus connections with each other. Once received the sensory inputs, the amygdaloid complex could generate the final output toward downstream target brain regions through the intra-amygdala network computation.

The amygdala receives information about the external environment from the thalamus and sensory cortex, which project primarily to the basolateral amygdala complex (BLA), as well as to the neighboring central amygdala (CeA). The BLA is reciprocally connected with cortical areas, especially the midline and orbital prefrontal cortices (PFCs), the hippocampus (HPC), and the sensory association areas.

Additionally, the CeA directly receives the nociceptive inputs from the lateral parabrachial nucleus (lPB). Taken together, the CeA integrates the information from BLA or other brain regions to generate the final output, which in turn results in the behavioral expression.

1b. The information flow of the amygdala in fear processing

One of the well-established test for the functional role of the amygdala in fear behavior is the classical fear conditioning (Killcross et al.,1997; Ledoux et al.,1988). The classical fear conditioning is a kind of associative learning pioneered by Ivan Pavlov in the 1920s in order to let animals to predict aversive events. Pavlovian fear conditioning is normally pairing an initially neutral stimulus (conditioned stimulus; CS), such as pure tone, with a noxious unconditioned stimulus (US), typically a foot shock with several times. As a consequence, the CS will acquire the ability to elicit conditioned fear responses (CR) like freezing, when presented alone in the retrieval trial.

There are extensive studies regarding to dissect the cellular mechanisms of the information flow of the fear processing (Smith and Pare, 1994; Woodfruff and Sah,

2007; Ciocchi et al., 2010; Wolff et al., 2014). The fear processing in the amygdala consists of convergence of synaptic inputs about the CS (auditory stimuli) and US (nociceptive stimuli), leading to the potentiation of synapses conveying CS information to the LA (Romanski et al., 1993). As a result, LA neurons would respond more strongly to the CS, and thus strengthen their projections to the CeA and the amygdala downstream output such as brainstem, triggering the CR (Han et al., 2007). Thus, in the original model, BLA was assumed as the main input station of the amygdala for CS information (Fig. 1A), whereas the CeA was thought of as the main output station of the amygdala for conditioned fear responses (Ledoux, 2000; Pare and Duvarci, 2012).

Recent studies suggested a revised model of the fear information flow that one or more population(s) of cells relay CS information to CeM (Pitkänen et al., 1997; Sah et al., 2003; Wolff et al., 2014). The anatomical literature suggested three potential candidates (Fig. 1B): the glutamatergic cells of the basal nucleus of BLA (BA) and the GABAergic neurons in the lateral subdivision of CeA (CeL) and intercalated cell mass (ICM) (Pare and Duvarci, 2012). The working model of fear information processing from the LA was tightly gated through both excitatory and inhibitory intra-amygdala transmission.

1c. Amygdala network-related emotional behaviors

Aside from the classical fear conditioning, previous studies revealed the effects of amygdala lesions on other emotional behaviors besides fear conditioning. In parallel to early studies on fear conditioning, amygdala lesions can also impair reward-based behavior (Cador et al., 1989; Everitt et al., 1989; Fig. 2). Another example is the anxiety-like behavior, previous studies revealed the role BLA–CeA projection is critical in the anxiety-like behavior. Activation of BLA-CeA pathway will lead to the increase of the anxiety level (Tye et al., 2011). In addition, optically activating BLA projections toward the ventral HPC (vHPC) is anxiogenic, whereas photostimulation of BLA inputs in the anterodorsal BNST (adBNST) is anxiolytic. In addition, photostimulation of the BLA-vHPC pathway also decreases social interaction (Felix-Ortiz et al., 2013; Felix-Ortiz and Tye, 2014).

2. Neuronal organization of different nuclei of the amygdala

The amygdala is comprised of a heterogeneous collection of nuclei, some with cortical properties, while others like the striatum. There are several nuclei which

are classified not only by the anatomical features but also by the differential roles in regulating the conditioned fear: the BLA, the ICMs, and the CeA. Despite the studies focusing on the functional consequence of these nuclei toward the behavior outcome, there are increasing studies trying to dissect the local circuit connections and cell types within the individual nucleus (Pare and Duvarci, 2012; Duvarci and Pare, 2014; Wolff et al., 2014; Fig. 1C).

2a. The basolateral amygdala complex

The BLA is a cortical-like structure, which is composed of 90% glutamatergic principal neurons (PCs) and 10% local inhibitory GABAergic neurons. According to previous studies, the BLA PCs reveal the heterogeneity either in the received inputs or the output regions. One population of the BLA PCs project to medial subdivision of CeA (CeM) whereas another populations target to the nucleus accumbens (NAc) would separately mediate positive and negative associative memory (Namburi et al., 2015).

Only about 10% of the BLA neurons are GABAergic neurons, which differ in the both electrical and morphological properties. There are at least four electrical distinct classes of BLA GABAergic neurons including accommodating, stuttering,

delay-firing, and fast spiking interneurons (Chiang et al., 2015). Moreover, the BLA GABAergic neurons can also be identified by the molecular marker it expressed. The two major groups are the parvalbumin (PV) and somatostatin (SOM) expressing neurons, which provide perisomatic and dendritic inhibition to the BLA principle neurons, respectively (Wolff et al., 2014).

The major outputs of the BLA principal neurons include the striatum, especially the NAc, and the BNST and the CeA. These downstream targets of the BLA have been considered as mediating the translation of BLA signals to behavioral output via the inter-nucleus inhibition (Janak and Tye, 2015; Fig. 1C).

2b. The Intercalated cell masses

ICM is composed of several small dense cell clusters located within the external and intermediate capsules of the amygdala (Likhtik et al., 2008; Ehrlich et al., 2009). The ICM cells are divided into the lateral ICM (ICM_L) and medial ICM (ICM_M). ICM_M can be further separated to medial dorsal (ICM_{MD}) and medial ventral (ICM_{MV}) parts, based on their relative anatomical locations. Compared to neighboring BLA principal neurons, ICM_L neurons have smaller soma size. Most ICM cells are

GABAergic neurons that receive both cortical and BLA inputs, and are considered to provide both feed-forward and feedback inhibition to BLA principal neurons and thus shape the output activity of the BLA (Fig. 1C). A small part of ICM_M neurons reciprocally connect with BLA principal neurons and thus provide the feedback inhibition of the BLA outputs (Duvarci and Pare, 2014; Asede et al., 2015). Since that, the ICM neurons are thought of as an inhibitory interface between the input (BLA) and output (CeA) nuclei of the amygdala. Recent evidence suggests that ICM_{MD} may participate in fear and extinction learning and processing of emotional stimuli (Busti et al., 2011; Palomares-Castillo et al., 2012).

2c. The central amygdala

The CeA is another inhibitory core in the amygdala consists of over 90% GABAergic neurons with the medium spiny neuron-like morphology. The central amygdala (CeA) is composed of at least two subdivisions: lateral (CeL) and medial (CeM) subdivisions. The output target brain regions of CeL are the CeM and periaqueductal gray (PAG), which play the role as downstream fear effectors controlling fear expression such as freezing (Knobloch et al., 2012).

A number of recent studies shed new light on the CeL undertaking an active role in the acquisition, consolidation, and extinction of conditioned fear (Wilensky et al., 2006; Ehrlich et al., 2009; Ciocchi et al., 2010; Pare and Duvarci, 2012; Li et al., 2013). The CeL neurons have different functional and molecular features (Cassell et al., 1999; Martina et al., 1999; Lopez de Armentia and Sah, 2004; Ciocchi et al., 2010; Haubensak et al., 2010; Amano et al., 2012; Li et al., 2013). By making reciprocal inhibitory connections, these neurons provide both feedforward and/or feedback inhibition within the CeL (Ciocchi et al., 2010; Haubensak et al., 2010; Li et al., 2013; Fig. 1C). Recent optogenetic approaches have demonstrated that intra-CeL inhibition can gate the output of the CeL and therefore controls the function of CeM and the expression of fear (Ciocchi et al., 2010; Haubensak et al., 2010; Pare and Duvarci, 2012). There are two largely non-overlapping and functional distinct groups of CeL neurons expressing different markers: somatostatin (SOM) and protein kinase C-δ (PKC-δ) (Haubensak et al., 2010; Li er al., 2013). Most CeL SOM^+ neurons provide local inhibition with only a small population (~20%) that directly projects to the PAG (Penzo et al., 2014). In contrast, the CeL PKC-δ^+ neurons, acting as the CeL_{off} cells in the retrieval of fear learning, serve as the major output neurons to the downstream CeM neurons and participate in the generation of CS evoke freezing behavior and the appetite control (Haubensak et al., 2010; Cai et al.,2014). In addition, the expression of oxytocin

receptor on the membrane of CeL PKC-δ^+ cells also participates in the regulation of fear expression (Ciocchi et al., 2010; Knobloch et al., 2012).

Another subnucleus of CeA, CeM, acts as one of the final output station of the amygdala and the neuronal activity is tightly controlled by the upstream excitatory inputs from BA and inhibitory inputs from ICM and CeL (Duvarci and Pare, 2014). Unlike the CeL neurons, most CeM neurons have a large soma, dendrites that branch sparingly and exhibit a low to moderate density of dendritic spines (Hall, 1972; Viviani et al., 2011). There are two major types of CeM neurons: low-threshold bursting (LTB) and ES neurons (Chiang et al., 2015). In addition, CeM neurons project to distinct downstream targets. One population of CeM neurons, with the oxytocin receptor expression, targets to dorsal vagal complex (DVC) and influence the breath rate and heartbeat rate, whereas another population targets the PAG to determine the fear expression such as freezing (Viviani et al., 2011; Knobloch et al., 2012).

3. The endocannabinoid signaling

3a. The endocannabinoid (eCB) signaling in the central nervous system

One of the best-known mechanism to mediate the neurotransmission and affect the synaptic plasticity is through the cannabinoid modulation. The eCB signaling in the brain and the body plays a central role in the control of stress, fear and anxiety. Modulation of synaptic processes the eCB system is widely distributed in the central nervous system, constituting a complex signaling system that provides multiple modes of synaptic transmission modulation.

The eCB system classically includes cannabinoid receptor type 1 (CB_1R) and type 2 (CB_2R), their endogenous lipid ligands (arachidonoyl glycerol (2-AG) and N-arachidonoylethanolamine (AEA)), and the eCB-synthesizing and -degrading enzymes.

In the central nervous system, initiation of eCB signaling results in retrograde inhibition of afferent neurotransmission. Postsynaptic eCB synthesis initiated via either voltage-dependent calcium channel (VGCC) activation or G-protein coupled receptor (GPCR)-dependent pathways would cause the release and diffusion of eCBs into the synaptic cleft (Kano et al., 2009). Thereafter, eCBs would bind to the CB_1R localized

to axon terminals of neurons, and thus activate the intracellular downstream signaling of Gi/o proteins and cause either short-term or long-term suppression of vesicular neurotransmitter release (Chevaleyre et al., 2006).

In many brain areas such as cortical regions and HPC, CB_1R is highly expressed in cholecystokinin (CCK)-expressing GABAergic interneurons. In addition, only low levels of CB_1R expression are present in glutamatergic neurons of cortical regions.

3b. The eCB signaling in the amygdala

The eCB system is expressed at some synapses in all brain regions that are important for the processing of anxiety, fear and stress, also including the amygdala nuclei: the BLA and the CeA.

In BLA, eCB could decrease evoked and spontaneous GABAergic synaptic transmission onto BLA principal neurons. Similarly, application of CB_1R agonist WIN 55212 produced a reduction in both frequency and amplitude of sIPSCs recorded from BLA principal neurons (Ramikie and Patel, 2012).

In CeA, recently studies provided the evidence that the glutamatergic inputs onto the CeL neurons is modulated by eCB signaling through multiple mechanisms (Ramikie et al., 2014), while there is a large variation of the effect of the WIN 55212 on the inhibitory inputs to the CeL neurons (Ramikie et al., 2014). Previous studies revealed that WIN 55212 resulted in the reduction of eIPSP amplitude from CeM neurons (Roberto et al., 2010).

4. Specific aims of this study

The CeL is known to play an important role in the emotional processing and consist of diverse GABAergic neuronal classes, but the synaptic organization of local inhibitory circuits in this region is largely unknown. By performing whole-cell recordings, I dissected the electrical composition of CeL neurons at the single cell level, and further investigated unitary transmission within the network organization of the CeL microcircuit by paired recordings.

4a. Aim 1: Characterization of the electrical and morphological properties of the

mouse CeL neurons.

With the increasing importance of the CeL region in multiple emotional behaviors and disorders, there are optogenetic approaches that separating the functional subpopulations of CeL neurons (Haubensak et al., 2010; Tye et al., 2011; Li et al., 2013). The functional CeL cell populations are divided based on either the distinct neuropeptides regulation on the cell, such as oxytocin and eCB signaling, or the differential expression level of molecular markers such as PKC-δ and SOM (Haubensak et al.,2010; Viviani et al., 2011; Knobloch et al., 2012; Li et al., 2013). However, the electrical properties, ion channel composition, and the functional connectivity of CeL neurons still remain unclear. To address this question, I firstly recorded the electrical properties from random CeL neurons and then performed *post hoc* reconstruction and statistical analysis of the recorded CeL cells.

4b. Aim 2: The functional connection and composition of CeL synapses

Recently studies focus on the functional role of CeL neurons in the emotional behaviors (Haubensak et al.,2010; Knobloch et al., 2012; Li et al., 2013). Although

optogenetic approaches make it easy to confirm the intra-CeL connections between different subpopulations of CeL cells by simultaneously activating a large amount of CeL synapses, the exact connectivity, synaptic properties, and short term dynamics of synapse formed by CeL neurons are unclear. By performing paired recording, I can investigate the unitary GABAergic transmission between CeL neurons.

4c. Aim 3: The neuromodulation and functional impact of CeL synapses on the CeL neural activity

Previous studies focus on the plastic change and neuromodulation of the excitatory transmission onto the CeL (Li et al., 2013; Penzo et al., 2014; Penzo et al., 2015). and thus switch the activity of CeL neurons to alter the output toward the downstream CeM and PAG. However, little is known about the eCB modulation on the CeL inhibitory synapses and what is the functional entertainment of the intra-CeL connections. To probe the important question, I used paired recordings to observe how the CeL synapses shape the activity of the postsynaptic cells. Furthermore, by delivering the induction protocol of the depolarization induced suppression of inhibition (DSI), I tried to detect the eCB mediated synaptic modulation of the CeL

synapses.

Chapter 2 | Functional organization and synaptic diversity in the amygdala inhibitory network

1. Introduction

The amygdala plays an important role in associative fear learning (LeDoux, 2007; Ehrlich et al., 2009; Johansen et al., 2011). A classical form of this learning is fear conditioning, in which animals learn to associate a neutral conditioned stimulus with an aversive unconditioned stimulus (Maren, 2001; Johansen et al., 2011). Both conditioned stimulus and unconditioned stimulus inputs converge to the LA, which then projects to the CeA through direct and indirect connections in other amygdala regions (Pitkanen et al., 1997; Amano et al., 2010; Johansen et al., 2011).

The CeA comprises the lateral (CeL) and medial (CeM) subdivisions. CeL neurons project onto the downstream CeM "output" neurons, which finally drive the expression of conditioned fear responses via projections to the brainstem and hypothalamus (Viviani et al., 2011). Therefore, the CeL is a relay station between the amygdala complex and downstream fear effectors (Pare´ et al., 2004; Sigurdsson et al.,

2007; Johansen et al., 2011).

A number of recent studies shed new light on the CeL undertaking an active role in the acquisition, consolidation, and extinction of conditioned fear (Wilensky et al., 2006; Ehrlich et al., 2009; Ciocchi et al., 2010; Pare and Duvarci, 2012; Li et al., 2013).

The CeL microcircuit consists of mostly GABAergic inhibitory neurons with different functional and molecular features (Cassell et al., 1999; Martina et al., 1999; Lopez de Armentia and Sah, 2004; Ciocchi et al., 2010; Haubensak et al., 2010; Amano et al., 2012; Li et al., 2013). By making reciprocal inhibitory connections, these neurons provide both feedforward and/or feedback inhibition within the CeL (Ciocchi et al., 2010; Haubensak et al., 2010; Li et al., 2013). Recent optogenetic approaches have demonstrated that intra-CeL inhibition gates CeL output and therefore controls the function of CeM and the expression of fear (Ciocchi et al., 2010; Haubensak et al., 2010; Pare and Duvarci, 2012). The CeL contains diverse GABAergic neuron classes, but the synaptic organization of local inhibitory circuits in this region is largely unknown.

Here I performed multiple whole-cell patch-clamp recordings from CeL neurons in mouse slices and investigated their synaptic connections. I found that two

major classes of CeL neurons with distinct firing patterns, namely the ES and the LS neurons, form two functionally distinct types of autapses. The efficacy of autaptic transmission in ES neurons was greater and was able to enhance spike-timing precision. Furthermore, brief depolarization of postsynaptic cells rapidly induced CB_1R-mediated suppression of output synapses of the presynaptic ES cells, but not the LS cells. Although CeL neurons are mutually connected, they prefer to form synapses with the different class. Intriguingly, presynaptic versus postsynaptic cell-type identities strongly dictate the efficacy and short-term plasticity (STP) of the CeL synapses. Synapses formed by different classes of cells are strong and markedly depressing when activated at 20 Hz. However, those synapses between cells of the same class are weak and do not exhibit prominent facilitation or depression. Such cell-type-specific transmission, modulation, and connectivity are likely to be critical for amygdala network function.

2. Materials and Methods

2a. Animals

The *Som-IRES-cre* mice (Taniguchi et al., 2011) and the *Ai14* reporter mice (Madisen et al., 2010) were purchased from the Jackson Laboratory (Bar Harbor, ME). The CB_1R-knockout (KO) mice were derived from a stock of genotyped animals that were provided by Dr. Zimmer (Zimmer et al., 1999). All mice were bred onto the C57BL/6J genetic background. Male mice (postnatal 3–8 weeks) were used for all the experiments. Animal procedures were carried out in accordance with the National Institutes of Health Guide for the Care and Use of Laboratory Animals. The experimental protocol was reviewed and approved by the Institutional Animal Care and Use Committee of National Yang-Ming University.

2b. Electrophysiological slice recording

Animals were sacrificed by rapid decapitation by appropriately trained researchers. In brief, their brains were rapidly removed, and 300–350 μm thick coronal sections were prepared with a vibratome (DTK-1000; Dosaka) using ice-cold sucrose-based solution containing (mM) 87 NaCl, 25 $NaHCO_3$, 1.25 NaH_2PO_4, 2.5 KCl, 10

glucose, 75 sucrose, 0.5 $CaCl_2$, and 7 $MgCl_2$, bubbled with 95% O_2/5% CO_2, pH 7.4. Slices were then transferred to the same solution at 34 ℃ for at least 30 min and allowed to cool naturally to room temperature. During experiments, slices were placed in a recording chamber and continuously superfused (~ 4 ml/min) with oxygenated ACSF containing (mM) 125 NaCl, 25 $NaHCO_3$, 1.25 NaH_2PO_4, 2.5 KCl, 25 glucose, 2 $CaCl_2$, and 1 $MgCl_2$. The CeL, which is delimited by bundles of axons, was identified with trans-illumination as previously described (Lopez de Armentia and Sah, 2004). Neurons in the CeL were then selected under visual control using infrared differential interference contrast (IR-DIC) videomicroscopy (Olympus BX51WI equipped with a charge-coupled device camera, DAGE IR-1000). To test the autaptic transmission, 20-Hz trains of five action potentials (APs) or depolarizing voltage steps were delivered to recorded cells. Paired or triple recordings were initiated by establishing a whole-cell recording from a CeL neuron, then testing its connectivity with as many as neighboring CeL neurons as possible within 100 μm somatic distance. To test the electrical coupling between CeL neurons, 1-s current (–50 pA) injections were delivered to one CeL neuron and the voltage responses were simultaneously recorded from the other cell. To induce the DSI, after 2 min baseline, the postsynaptic CeL neurons were depolarized to 0 mV for 10 s. Whole-cell patch-clamp recordings were made with a Multiclamp 700B amplifier (Molecular Devices). Recording electrodes (2–6 MΩ) were pulled from

borosilicate glass (outer diameter, 1.5 mm; 0.32 mm wall thickness; Harvard Apparatus). Pipette capacitances of both electrodes were carefully compensated and series resistance was compensated using the automatic bridge balance (readouts after compensation were 6–18 MΩ). Signals were filtered at 4 kHz except where noted using the 4-pole low-pass Bessel filter. A Digidata 1440A connected to a personal computer was used for stimulus generation and data acquisition. The sampling frequency was 10 kHz. Pulse sequences were generated by pCLAMP 10.2 or 10.3 (Molecular Devices). The recording temperature was 24 ± 2 °C, except a subset of STP experiments (see Fig. 8) was at 35 ± 2 °C.

2c. Solutions and drugs

The majority of whole-cell patch-clamp recordings was made with the intracellular solution containing (mM) 144 KCl, 0.2 EGTA, 4 MgATP, 10 HEPES, 7 Na_2-phosphocreatine, 0.1 GTP, and 0.4% biocytin; pH adjusted to 7.3 with KOH. For the experiments of investigating the inhibitory effect on neuronal output, I used a low Cl^- internal solution containing (mM) 136.8 K-gluconate, 7.2 KCl, 0.2 EGTA, 4 MgATP, 10 HEPES, 7 Na_2-phosphocreatine, 0.5 Na_3GTP (pH 7.3 with KOH), and 0.4% biocytin. In a subset of experiments, one or more of the following antagonists (Sigma

unless otherwise indicated) was also added to the ACSF: 2 mM kynurenic acid to block AMPA and NMDA receptors; 1 μM gabazine (Tocris) to block $GABA_A$ receptors. K_v channel blockers 4-amino-pyridine (4-AP; Sigma-Alderich) and α-dendrotoxin (α-DTX; Alomone Labs) were also applied in the presence of synaptic blockers (with additional 0.5% bovine serum albumin (UniRegion Bio-Tech) for α-DTX) via bath superfusion.

2d. Hierarchical clustering analysis

To classify the cells, an unsupervised clustering analysis (Cauli et al., 2000; Jasnow et al., 2009; Sosulina et al., 2010) was performed by using squared Euclidean distances and Ward's method (Ward, 1963). Electrophysiological properties of CeL cells were tested for uniformity in their distributions. Each of the quantified 14 variables (listed in Table 1) was binned and tested by the D'Agostino–Pearson normality test, which is based on the assumption that a variable is normally distributed in a class. Variables with a non-Gaussian distribution were used for subsequent unsupervised clustering. Hierarchical clustering arranges data items into a tree-like dendrogram, in which tree leaves represent data items, and the length of tree edges between leaves represents the dissimilarity between data items. Tree leaves belonging to a subtree

suggest high similarity and therefore form a group. Hierarchical clustering operates as follows. First, each CeL neuron was transformed into a 4-dimensional data point with variables of spike delay, ramp ratio, resting membrane potential (RMP), and rheobase. Before clustering, I first normalized variables into the range (0, 1) by performing min–max normalization. The distance between data points represents the dissimilarity between them; closer data points have higher similarity. Next, I clustered all the data points by the following iterative procedure: First, assign each data point to a cluster; every cluster therefore contains only one data point. Second, merge the two closest clusters into one cluster; hence, there is one cluster fewer than previously. Third, determine the distance between the new cluster and each of the old clusters. Fourth, repeat steps two and three until there is only one cluster left. Ward's method linkage rules (Ward, 1963), which minimizes the error sum of squares of any pair of cluster in step three. The pair of clusters with minimum between-cluster distance are merged. The hierarchical clustering analysis was carried out with the Free Statistics Software (Wessa, 2016; Free Statistics Software, Office for Research Development and Education, version 1.1.23-r7, URL http://www.wessa.net/).

2e. Sholl analysis

Sholl analysis (Sholl, 1953) was used to investigate dendritic complexity in relation to their distance from the soma. Briefly, concentric Sholl segments (concentric radial interval: 25 μm) were generated starting at a distance of 10 μm from the center of soma. The number of process intersections and dendritic length were analyzed per Sholl segment, respectively.

2f. Recovery of biocytin-filled neurons

Neurons were filled with biocytin (0.2–0.4%) during recordings. After more than 30 min recording, slices were fixed overnight with 4% paraformaldehyde in phosphate-buffered solution (PBS; 0.1 M, pH 7.3). Following wash with PB, slices were incubated with fluorescein isothiocyanate (FITC)-conjugated avidin-D (2 μl/ml; Invitrogen, Eugene, Oregon) in PB containing 0.3% triton X-100 overnight at 4 ˚C. After wash, slices were embedded in a mounting medium Vectashield® (Vector Laboratories, Burlingame, CA).

2g. Image acquisition and anatomical reconstruction

For 3-D reconstruction of biocytin-labeled cells, high-resolution two-photon images of neurons were acquired. Labeled neurons were examined by a two-photon microscope using a pulsed titanium: sapphire laser (Chameleon-Ultra II tuned to 800 nm; Coherent, Portland, OR) attached to a Leica DM6000 CFS (Leica, Wetzlar, Germany) that was equipped with a 63×/0.9 numerical aperture (NA) water immersion objective (objective type HCX APO L). The morphology of the cells was reconstructed from a stack of 121-165 images per cell (voxel size, 120-378 nm in the x-y plane; 1 μm along the z-axis). Image stacks belonging to one cell were imported into the Neuromantic 1.6.3 software (Myatt et al., 2012) for 3-D reconstruction. Analysis of morphological parameters was performed using Neurolucida Explorer (MicroBrightField, Williston, VT).

2h. Data analysis and statistics

Data were analyzed using Clampfit 10.3 (Molecular Devices) and Prism 5.0 or 6.0 (GraphPad). The rheobase is the minimal intensity of 2-s current pulse required for action potential (AP) generation. Briefly, neurons were held at –70 mV and depolarizing current steps (step increment 1 pA) were injected to induce APs. The spike delay was measured from the start of square depolarizing current pulse injection to the

peak of the first AP evoked by the rheobase. The ramp ratio is the averaged membrane potential (V_m) between 0.2 to 0.25 s following the onset of subthreshold current pulse (intensity: 1 pA less than the rheobase; 2 s) injection versus the averaged V_m between 1.8 to 1.85 s. The input resistance (R_N) was measured by the ratio of the steady-state (the last 100 ms) voltage response versus the injected 1-s hyperpolarizing (10 pA) current pulse. The membrane time constant (τ_m) was calculated using a single-exponential fit to the late portion of the voltage change produced by hyperpolarizing (50 pA) current pulse injection in the current clamp mode at the RMP. The spike threshold was measured as the voltage at which the first derivative of voltage exceeded the threshold (20 V/s). The synaptic latency was measured from the peak amplitude of the AP to the 10% rise time of the unitary inhibitory postsynaptic current (uIPSC) (Liu et al., 2014); the decay time constant of the uIPSC was fitted with a single exponential. The postsynaptic traces in the figures were averages of > 8 sweeps. The DSI response was quantified by normalizing the average uIPSC peak amplitude in the following 30 s right after the depolarization to that of the baseline uIPSC. The Fisher's exact test was used for statistical comparison of the connectivity probabilities as a previous study (Böhm et al., 2015). Data were presented as mean ± standard error of mean (SEM). Error bars equal SEM and were plotted only when they exceeded the respective symbol size. Since the normality of underlying distributions of variables in both groups is not

known (Walker, 2002), I determined statistical significance by the Wilcoxon rank-sum (between groups of cells) or Wilcoxon signed-rank test (within groups of cells). Comparisons between multiple groups were tested by one-way ANOVA (with Tukey's *post hoc* test) or two-way ANOVA test (with Bonferroni *post hoc* test). The significance of correlation between the first uIPSC$_1$ peak amplitude and multiple-pulse ratio/failure rate was determined by computing the Spearman rank correlation coefficient (r_s) and testing it against tabulated values (Spearman, 1904).

3. Results

3a. The CeL neurons comprise two major functionally distinct populations

The amygdala is comprised of several distinct nuclei (Fig. 3A). In acutely prepared mouse amygdala slices, I can identify the CeL region by the surrounding axon bundles with the IR-DIC optics (Fig. 3B) as previously described (Lopez de Armentia and Sah, 2004). Neurons in the CeL display heterogeneous intrinsic excitability (Martina et al., 1999; Lopez de Armentia and Sah, 2004; Chieng et al., 2006; Haubensak et al., 2010; Amano et al., 2012; Chiang et al., 2015). We first performed whole-cell patch-clamp recordings on cells and then made *post hoc* morphological reconstructions

of the recorded cells. In agreement with previous results (Haubensak et al., 2010; Li et al., 2013), the majority (approximately 96%; 217 of 225; Fig. 3C) of CeL neurons exhibited either the ES or the LS phenotype in response to depolarizing current steps, whereas only a small subset (3.5%; 8 of 225; Fig. 3C) displayed the LTB phenotype (Chieng et al., 2006). Because the onset of spikes varied in response to different current injections, I determined the spike delay (Fig. 3D) of the first AP upon a just suprathreshold current (i.e., rheobase) injection. Moreover, I determined the first AP properties, including the peak amplitude, voltage threshold, half-width, maximal rising rate, and maximal falling rate. In addition to AP phenotypes, ES and LS cells differed in their subthreshold membrane responses (Fig. 3D). In striking contrast to ES cells, LS cells exhibited a slow ascending ramp in response to subthreshold current injection and displayed a greater ramp ratio (Table 1).

To further test whether ES and LS cells arise from two separate classes of CeL neurons or whether they represent a single population of cells spanning a continuum of excitability, I analyzed several other physiological features (Table 1) from all non-LTB neurons. Overall, four features (spike delay, ramp ratio, RMP, and rheobase) showed non-Gaussian distributions (Fig. 3E).

To divide these two distinct cell classes unbiasedly, I performed hierarchical

cluster analysis from 185 randomly recorded CeL neurons based on these four features (Cossart et al., 2006; Graves et al., 2012; also see Materials and Methods). Strikingly, the cluster dendrogram yielded two distinct neuron populations, i.e., LS and ES cells (Fig. 3F). The spike delay of LS and ES neurons was 1762 ± 23 ms (blue, n = 105) and 626 ± 68 ms (red, n = 80), respectively ($p < 0.0001$; Wilcoxon rank-sum test; Table 1). In addition, the LS population exhibited a more hyperpolarized RMP and a larger rheobase (Table 1). Similar to the dendrogram, the scatter-plot of spike delay vs. ramp ratio revealed two distinctly nonoverlapping clusters (Fig. 3G). Classification of cells with the arbitrary cutoff value (spike delay of 1.5 s) fell into two categories, which corresponded to the same two populations determined by the unbiased hierarchical cluster analysis. As a result, I classified neurons with a spike delay of > 1.5 s at rheobase as the LS cells, and the remainders as the ES cells in the subsequent experiments of this study.

3b. LS and ES cells show differential sensitivity to the Kv1 channel blocker α-dendrotoxin

A rich repertoire of ion channels shape the firing pattern of mammalian

central neurons (Martina et al., 1998; Lien et al., 2003; Bean, 2007). Delayed or late-firing cells display a remarkably long delay to the initiation of the first AP. Moreover, application of long depolarizing steps to near the firing threshold gives rise to a long depolarizing ramp, suggesting the expression of slowly inactivating D-type K^+ current (I_D) (Storm, 1988; Martina et al., 1998; Goldberg et al., 2008; Kirchheim et al., 2013). The I_D is largely mediated by low-threshold voltage-gated voltage gated K^+ channel type 1 (Kv1) family, which is sensitive to low concentrations of 4-AP (for instance, 30 μM), a broad-spectrum K^+ channel blocker and α-DTX (100 nM), a specific Kv1 blocker (Martina et al., 1998; Dodson et al., 2002; Goldberg et al., 2008; Mathews et al., 2010; Kirchheim et al., 2013). We thus tested the effects of these pharmacological agents on the spike latency and depolarizing ramp. Indeed, bath application of 30 μM 4-AP significantly shortened the spike delay in LS cells (control, 1874 ± 34 ms vs. 4-AP, 993 ± 103 ms, $n = 13$; $p < 0.001$; Wilcoxon signed-rank test; Fig. 4A left traces and Fig. 4C left), but not in ES cells (control, 411 ± 129 ms vs. 4-AP, 412 ± 134 ms, $n = 7$; $p = 0.81$; Wilcoxon signed-rank test; Fig. 4B left traces and Fig. 4C left). In line with this, a low concentration of 4-AP (30 μM) significantly increased the input resistance of LS cells (control, 351 ± 16 MΩ vs. 4-AP, 395 ± 20 MΩ, $n = 7$; $p < 0.05$; Wilcoxon signed-rank test), but not that of ES cells (control, 380 ± 19 MΩ vs. 4-AP, 373 ± 17 MΩ, $n = 6$; $p = 0.99$; Wilcoxon signed-rank test; data not shown). Similarly, α-DTX

(100 nM) significantly decreased the spike latency in LS cells (control, 1845 ± 40 ms vs. α-DTX, 1306 ± 149 ms, $n = 9$; $p < 0.01$, Wilcoxon signed-rank test; Fig. 4A right traces and Fig. 4C left), but not in ES cells (control, 584 ± 164 ms vs. α-DTX, 567 ± 138 ms, $n = 6$; $p = 0.84$, Wilcoxon signed-rank test; Fig. 4B right traces). Furthermore, both 4-AP (30 μM) and α-DTX (100 nM) preferentially reduced the ramp ratio in LS cells (control, 1.45 ± 0.05 vs. 4-AP, 1.15 ± 0.05, $n = 13$; $p < 0.001$, Wilcoxon signed-rank test; Fig. 4C middle; control, 1.36 ± 0.06 vs. α-DTX, 1.22 ± 0.05, $n = 9$; $p < 0.05$, Wilcoxon signed-rank test; Fig. 4C middle). These effects are consistent with findings in other brain regions (Goldberg et al., 2008; Campanac et al., 2013) where Kv1 channel blockade converted the LS cells to the ES-like phenotype.

Aside from the firing pattern, various types of K^+ channels regulate neuronal excitability for spike generation. Indeed, 4-AP reduced the rheobase current in both LS and ES cells (LS cell, control, 40.4 ± 5.5 pA vs. 4-AP, 26.2 ± 6.6 pA, $n = 13$; $p < 0.05$, Wilcoxon signed-rank test; Fig. 4C right; ES cell, control, 43.7 ± 9.1 pA vs. 4-AP, 20.4 ± 4.5 pA, $n = 7$; $p < 0.05$, Wilcoxon signed-rank test; Fig. 4C right). In contrast, α-DTX, a specific Kv1 blocker, selectively reduced the rheobase in LS cells, but not in ES cells (LS cell, control, 38.7 ± 9.2 pA vs. α-DTX, 31.1 ± 9.4 pA, $n = 9$; $p < 0.01$, Wilcoxon signed-rank test; Fig. 2C right; ES cell, control, 40.7 ± 6.4 pA vs. α-DTX, 28.2 ± 6.7

pA, n = 6; p = 0.07, Wilcoxon signed-rank test; Fig. 4C right). These findings further corroborate the notion that Kv1 is preferentially expressed in LS cells.

3c. LS and ES cells have similar anatomical features

Aside from distinguishing electrophysiological characteristics, I next searched for differences in morphological characteristics between these functionally distinct neuronal populations. To address this question, I reconstructed biocytin-stained CeL neurons (Fig. 5A). Detailed morphometric analyses revealed that no consistent differences were found between LS and ES cells in the somatic size (LS cell, 16.7 ± 1.1 μm, n = 15 vs. ES cell vs. 17.4 ± 1.2 μm, n = 13; p = 0.57, Wilcoxon rank-sum test), total dendritic length (LS cell, 1514 ± 165 μm, n = 15 vs. ES cell, 1778 ± 273 μm, n = 13; p = 0.65, Wilcoxon rank-sum test), and total branch points (LS cell, 10.0 ± 0.9, n = 15 vs. ES cell, 11.4 ± 0.8, n = 13; p = 0.33, Wilcoxon rank-sum test). Furthermore, Sholl analysis (Sholl, 1953) revealed that the number of dendritic intersections (LS cell, n = 15; ES cell, n = 13; p = 0.36, two-way ANOVA test, Fig. 5B) and the length of dendrite segments (LS cell, n = 15; ES cell, n = 13; p = 0.39, two-way ANOVA test, Fig. 5C) were similar between these two neuronal populations. Thus, both neuronal types have a similar anatomical structure.

3d. LS and ES cells display distinct autaptic neurotransmission

GABAergic inhibitory neurons in the cortex can form self-innervating synapses, namely autapses, as previously reported (Tamás et al., 1997; Bacci et al., 2003; Connelly and Lees, 2010). In whole-cell current-clamp (Ic at –70 mV; $[Cl^-]_i$ = 144 mM; corresponding to E_{GABA} = 1.7 mV) recordings, I observed that APs in some CeL neurons were immediately followed by small slow membrane depolarization "bumps" (Fig. 6A). Such membrane bumps were blocked by gabazine (1 μM), suggesting $GABA_A$ receptor-mediated depolarizing autaptic IPSP present in CeL neurons. Similarly, fast inward Na^+ currents were also followed by slower gabazine-sensitive inward currents (decay τ, 36.6 ± 1.3 ms, n = 6) when cells were briefly depolarized from –70 to +20 mV in voltage-clamp (Vc) (Fig. 6B). The autaptic connection rates of LS cells and ES cells were 13% (13/98) and 19% (16 of 84), respectively (p = 0.43, Fisher's exact test; Fig. 6C). On average, the autaptic inhibitory postsynaptic potential (aIPSP) in ES cells was 8.0 ± 2.5 mV (n = 8) about 4-fold greater than that in LS cells (2.2 ± 0.4 mV; n = 6; p < 0.05, Wilcoxon rank-sum test; Fig. 6D, left). In line with this, the autaptic conductance (aIPSG) was 2.9 ± 1.1 nS (n = 10) in ES cells and 0.6 ± 0.3 nS (n = 9) in LS cells (p < 0.01, Wilcoxon rank-sum test; Fig. 6D, right). We next examined whether

ES and LS cells differed in their autaptic properties. Gabazine-sensitive aIPSPs or currents (aIPSCs) were evoked by trains of 5 APs at 20 Hz in the Ic configuration (Fig. 6E, F left) or 5 brief depolarization steps at 20 Hz in the Vc configuration (Fig. 6E,F right). As illustrated, aIPSPs or aIPSCs recorded in LS cells were slightly depressing (the ratio of 5th/1st response, 91 ± 11%, n = 16; Fig. 6E). In contrast, autaptic transmission in ES cells was strongly depressing (the ratio of 5th/1st response, 58 ± 11%, n = 18; Fig. 6F), significantly different from that in LS cells ($p < 0.01$, Wilcoxon rank-sum test; Fig. 6G). Overall, our data revealed that autaptic transmission in ES cells is robust but transient during 20-Hz trains of activation, compared to that in LS cells.

3e. Autaptic transmission enhances spike timing-precision in ES cells

GABAergic transmission results in hyperpolarization after single APs and thus set the timing of subsequent spikes in a train (Bacci and Huguenard, 2006; Woodruff and Sah, 2007). To investigate the physiological impact of autapses, neurons were held at –50 mV and were depolarized by repeated identical suprathreshold current injections to spike at 6–10 Hz. The timing of each spike in both neurons varied from trials to trials (Fig. 7A and B). We next compared the effect of autaptic transmission on spike-timing precision in LS cells versus ES cells. The analysis was restricted to the

aIPSC that was greater than three times the standard deviation of the preceding baseline when recorded at –50 mV ($[Cl^-]_i$ = 7.2 mM) in the Vc configuration. As previously described (Bacci and Huguenard, 2006), I quantified spike-timing precision as spike jitter, defined as the standard deviation of the ordinal spike times across multiple identical stimulation trials. Both LS and ES cells had progressive increases in the spike jitters (Fig. 7C). Notably, the spike jitter was significantly greater in LS cells than ES cell at the sixth spike in the train ($p < 0.001$, *post-hoc* Bonferroni test after two-way ANOVA; Fig. 7C). After blockade of GABAergic autaptic transmission, the jitter of each spike during a train of both autapse-containing CeL neuron types was modestly increased (1 μM gabazine; Fig. 7D). Notably, the jitter of the second spike in ES cells became significantly greater than that in LS cells ($p < 0.05$, *post-hoc* Bonferroni test after two-way ANOVA; Fig. 7D). Although there was a small increase of jitters in LS cells by gabazine application, this effect was not significant ($n = 5$, $p = 0.11$, two-way ANOVA test; Fig. 7E). In striking contrast, the jitters of the second and third spikes in ES cells were significantly increased by gabazine ($n = 5$, the normalized second spike jitter, 310 ± 50 % of control, $p < 0.001$; the normalized third spike jitter, 210 ± 40 % of control, $p < 0.05$; *post hoc* Bonferroni test after two-way ANOVA test; Fig. 7F). These results indicated that autaptic transmission in ES cells enhances the spike-timing precision during trains of activation.

Finally, I examined the impact of aIPSG on the second and third spike jitters. We first analyzed the correlation of aIPSG versus spike jitter in gabazine (normalized to the jitter of control). We found that the magnitude of aIPSG positively correlated with the jitter change after blockade of autaptic transmission by gabazine (Fig. 7G, H). Furthermore, the second spike-evoked aIPSGs in ES cells were 2-fold greater than those in LS cells (ES cell: 1.7 ± 0.3 nS for vs. LS cell: 0.8 ± 0.2 nS; $p < 0.05$; Wilcoxon rank-sum test; Fig. 7G). It is notable that although gabazine caused a small increase in the third spike jitter in ES cells, the third spike-evoked aIPSGs in ES and LS cells were quite similar (ES cell: 1.2 ± 0.3 nS for vs. LS cell: 0.9 ± 0.1 nS; $p = 0.34$; Wilcoxon rank-sum test; Fig. 7H). In sum, these results indicate that the efficacy of aIPSG may account for the cell type-specific enhancement of spike-timing precision.

3f. Presynaptic cell type dictates DSI

eCB signaling modulates synaptic transmission in the CeA (Roberto et al., 2010; Ramikie et al.,2014). However, only a few GABAergic terminals in the CeL are CB_1R positive (Ramikie et al., 2014). To address whether eCB specifically modulated GABA release of a specific cell type, I performed simultaneous paired recordings from

identified cell types and then applied a DSI protocol, known to trigger retrograde release of eCB and suppress phasic GABA release (Ramikie et al., 2014). Interestingly, I found that DSI was exclusively present at the synapses, in which presynaptic cells was the ES phenotype (Fig. 8A–C). Following the DSI induction, the uIPSC amplitude was immediately decreased by 73 ± 7% (n = 12) and gradually recovered to the baseline (Fig. 8C). The recovery time course was fitted with a mono-exponential function with a time constant of 39.3 s. As illustrated in a reciprocally connected ES and LS cell pair (Fig. 8D), I found a clear distinction: the DSI indeed occurred at the ES→LS synapse, but not at the LS→ES synapse. In sum, the DSI is independent of postsynaptic cell types, suggesting that eCB mobilization occurs in both ES and LS cells during the DSI induction (4 ES cells and 7 LS cells; Fig. 8C). Consistent with this notion, DSI was not present in CB_1-receptor knockout mice (Fig. 8E). Taken together, retrograde eCB signaling that selectively mediates short-term forms of plasticity at ES neuron output synapses (Fig. 8F) represents a biochemical substrate for functional segregation between ES and LS neuron types.

3g. CeL neurons are connected by chemical but not electrical synapses

We further examined the synaptic connections between these two types of CeL

neurons (Fig. 9A). Experiments were performed by first establishing a whole-cell recording from a CeL neuron, then testing its connectivity with as many neighboring CeL neurons as possible within 100 μm somatic distance. To facilitate measurement of synaptic currents, whole-cell recordings were made with high intracellular chloride solution ($[Cl^-]_i$ = 144 mM). Trains of five APs at 20 Hz were evoked every 10 s in the presynaptic neuron and responses were recorded in postsynaptic neurons at -70 mV in the Vc or Ic configuration. Figure 9B represents an example of chemical transmission between an ES cell, a presynaptic cell and an LS cell, a postsynaptic cell (ES→LS). The synaptic currents were precisely time locked to the presynaptic AP trains and were abolished following bath application of 1 μM gabazine (bottom traces, Fig. 9B), indicating $GABA_A$ receptor-mediated transmission. Similar results were found when postsynaptic cells were recorded under the Ic mode (data not shown). The peak amplitude of the first uIPSC ($IPSC_1$) evoked by the single presynaptic AP (the first AP in the train; Fig. 9B) was taken as an index of synaptic efficacy, the percentage of failures as a measure of the reliability of transmission. The distribution of uIPSC1 latencies of this example synapse showed an average peak latency of 1.48 ± 0.07 ms (average from 30 events; Fig. 9C, left), consistent with monosynaptic transmission. Synaptic properties including the 20-80% rise time, the decay time constant, the amplitude of average uIPSC1, and the failure rate for this connection were 0.66 ± 0.06

ms, 28.1 ± 2.2 ms, 156 ± 12 pA (average from 30 sweeps, including failures; Fig. 9C) and 6.6 %, respectively. Consistent with GABAergic transmission, I found that when the paired recordings were made on postsynaptic cells with different intracellular chloride concentrations, the measured reversal potentials of uIPSCs were close to the predicted equilibrium potentials for $GABA_A$ receptor-mediated currents (for $[Cl^-]_i$ = 2, 20, and 144 mM, E_{GABA} = -81.2, -45.3, 1.45 mV, respectively) (Fig. 9D).

In addition to the chemical transmission, I investigated whether CeL neurons formed electrical synapses as well. Sustained hyperpolarizing responses (~-15 mV; 1 s) were evoked in one randomly picked CeL neurons and we recorded the membrane potential change from other CeL neurons nearby. We tested three different types of CeL cell pairs (Fig. 10A-C). To my surprise, no electrically coupled responses were observed in all pairs (0 of 417).

3h. Both pre- and postsynaptic cell types determine synaptic properties

I next investigated whether each CeL neuron class forms synapses with highly specific temporal dynamics onto target neurons. To address this, I examined both divergent and convergent synapses using simultaneous triple whole-cell patch-clamp recordings. For the divergent connections (Fig. 11A), I elicited a train of 5APs at 20 Hz in a presynaptic neuron and simultaneously recorded uIPSCs were from two

different classes of postsynaptic neurons. I found that the ES→ES synapse was weakly depressing ($uIPSC_5/uIPSC_1$ = 0.86; Fig. 11A left), whereas the ES→LS synapse was strongly depressing ($uIPSC_5/uIPSC_1$ = 0.14; Fig. 11A right). These results indicate differential synaptic modifications via the same axon innervating two different targets (Markram et al., 1998; Buchanan et al., 2012; Sylwestrak and Ghosh, 2012; see review by Blackman et al., 2013). In an example of convergent synaptic connections (Fig. 11B), I recorded responses from a neuron innervated by two different classes of presynaptic neurons. Consistent with the above findings, the ES→ES synapse was weakly depressing ($uIPSC_5/uIPSC_1$ = 0.81; Fig. 11B left). Conversely, the LS→ES synapse was strongly depressing ($uIPSC_5/uIPSC_1$ = 0.31; Fig. 11B right). Thus, unlike those found in other brain regions where properties of inhibitory synapses were determined by either pre- or postsynaptic cell types (Geracitano et al., 2007; Ma et al., 2012; Blackman et al., 2013; Liu et al., 2014), the identities of both pre- and postsynaptic cells determined the properties of CeL inhibitory synapses.

In addition to unidirectional connections, I also detected bidirectional connections between CeL neurons. Consistent with the results obtained from pairs and triplets, synapses between two different classes were strongly depressing. As illustrated in Figure 11C, synapses between mutually connected ES and LS cells showed marked

depression (ES→LS, $uIPSC_5/uIPSC_1$ = 0.63; LS→ES, $uIPSC_5/uIPSC_1$ = 0.56; Fig. 11C). Conversely, synapses between cells of the same class showed weak plasticity (ES #1→ES #2, $uIPSC_5/uIPSC_1$ = 1.03; ES #2→ES #1, $uIPSC_5/uIPSC_1$ = 1.28; LS #1→LS #2, $uIPSC_5/uIPSC_1$ = 0.79; LS #2→LS #1, $uIPSC_5/uIPSC_1$ = 0.71; Fig. 11D, E).

In total, 66 of 588 pairs (11.2%) showed chemical synaptic responses. In contrast, I did not detect any electrically coupled response in all pairs (0 of 588). The connection rates of the LS→ES and ES→LS synapses were significantly higher than that of the LS→LS synapse (LS→ES group, 16.1% vs. LS→LS group, 6.3%; $p < 0.05$, Fisher's exact test; ES→LS group, 16.9% vs. LS→LS group, 6.3%; $p < 0.01$, Fisher's exact test; Fig. 9F), but were similar to that of the ES→ES synapse (LS→ES group, 16.1% vs. ES→ES group, 12.1%; $p = 0.55$, Fisher's exact test; ES→LS group, 16.9% vs. ES→ES group, 12.1%; $p = 0.45$, Fisher's exact test; Fig. 11F). Overall, the average distances between the soma of these four types of connections were not significantly different ($p = 0.97$, one-way ANOVA test; Fig. 11G). Therefore, preferential synapse formation between distinct cell types may be critical for microcircuits formed among inhibitory neurons.

Analysis of all CeL neuron pairs revealed that STP by a train of presynaptic stimulation at 20 Hz showed little depression at the ES→ES ($uIPSC_5/uIPSC_1$, 102 ± 10%) or LS→LS cell ($uIPSC_5/uIPSC_1$, 87 ± 5%) connection (Fig. 12A, B; Table 2). By contrast, the ES → LS or LS → ES cell connection showed strong multiple-pulse depression (ES → LS group, $uIPSC_5/uIPSC_1$, 29 ± 3%; LS → ES group, $uIPSC_5/uIPSC_1$, 30 ± 4%; Fig. 12C, D; Table 2). To examine if STP of CeL synapses was preserved at the physiological temperature, I also tested STP at 34 °C and found similar results. We thus pooled them in Figure 12.

Similar to STP, the synaptic efficacy (estimated by the amplitude of $uIPSC_1$) was also specific to pre- and postsynaptic cell classes (Table 2). On average, the $uIPSC_1$ amplitudes at the ES→ES (34.2 ± 3.9 pA, n = 10) and LS→LS (28.7 ± 5.2 pA, n = 15) synapses were significantly smaller than those at the LS→ES (145.4 ± 47.1 pA, n = 13) and ES→LS (177.2 ± 40.3 pA, n = 20) synapses ($p < 0.001$, one-way ANOVA test; Table 2). Consistently, the failure rate of evoking the $uIPSC_1$ at the ES→ES (44.0 ± 5.0%, n = 10) or LS→LS (40.0 ± 8.0%, n = 15) synapse was significantly greater than that at the ES→LS (14.0 ± 3.0%, n = 20) or LS→ES (16.0 ± 3.0%, n = 13) synapse ($p < 0.01$, one-way ANOVA test; Table 2). Moreover, the $uIPSC_1$ amplitude inversely correlated with the multiple-pulse ratio ($uIPSC_5/uIPSC_1$) by performing Spearman's

rank correlation coefficient (r_s) analysis (r_s = –0.50, p < 0.0001; Fig. 12E). This observation is consistent with the notion (Debanne et al., 1996) that strong synapses (e.g., the ES→LS or LS→ES synapse) with a high initial release probability exhibit strong depression during multiple stimulation at a high frequency. Similarly, the peak amplitude of $uIPSC_1$ was inversely proportional to the failure rate (r_s = –0.70, p < 0.0001; Fig. 12F).

3i. Cell type-specific STP is independent of the cell marker SOM

CeL neurons express neurochemical markers such as neuropeptide SOM or PKC-δ (Cassell et al., 1986; Haubensak et al., 2010; Li et al., 2013; Penzo et al., 2014., Penzo et al., 2015). SOM^+ and PKC-δ^+ neurons are largely nonoverlapping (Li et al., 2013). In order to further investigate if there is any correlation between the expression of SOM and the intrinsic electrical properties of CeL neurons, here I also identified SOM^+ neurons, which readily expressed the red fluorescent protein tdTomato, in the *Som-IRES-cre;Ai14* mice (Fig. 13A). I observed that both SOM^+ and SOM^- neurons exhibited a high degree of variation in the spike delay (Fig. 13B). Furthermore, cumulative distribution of spike delays from SOM^+ and SOM^- neurons showed a similar pattern (p = 0.11; Kolmogorov-Smirnov test). In agreement with a recent report (Li et

al., 2013), I found that 54% (14 of 26 cells, cells located left to the vertical dashed line) of SOM^+ cells were the ES phenotype (Fig. 13B), similar to that (55%; 12 of 22 cells) of SOM^- cells. Altogether, the neurochemical marker SOM did not correlate with intrinsic excitability.

We next sought to investigate synaptic connectivity and transmission between neurons based on the expression of SOM in the pre- and postsynaptic neurons. There were four types of connections and they displayed similar multiple-pulse depression ($SOM^+ \rightarrow SOM^+$, 52 ± 15%; $SOM^- \rightarrow SOM^-$, 59 ± 16%; $SOM^+ \rightarrow SOM^-$, 57 ± 16%; $SOM^- \rightarrow SOM^+$, 56 ± 13%; $p = 0.99$, one-way ANOVA test; Fig. 13C). Notably, if I presented the same dataset according to ES and LS cell phenotypes, the STP of these synapses was highly predictable from the presynaptic-postsynaptic interaction principle (LS→LS, 80 ± 5%; ES→ES, 124 ± 11%; LS→ES, 28 ± 3%; ES→LS, 33 ± 6%; $p < 0.0001$, one-way ANOVA test; Fig. 13D). These results indicate that the synaptic strength and STP of CeL synapses are independent of SOM expression.

3j. Cell type-specific STP controls output spike patterns

Finally, I tried to probe the functional consequences of the cell type-specific STP. I first obtained paired recordings from synaptically coupled pairs and

characterized their synaptic dynamics. Consistent with our observation, all recordings here showed that synapses between electrically heterogeneous neurons were strong and markedly depressing, whereas synapses between electrically homogeneous neurons were weak and slightly facilitating or depressing. Therefore, I classified synapses into a strong depressing synapse (Fig. 14A) versus a weak non-depressing synapse (Fig. 14B). We next elicited APs in postsynaptic neurons by trains of brief current injections at 20 Hz. The magnitude of brief current injection was adjusted such that firing probabilities were kept at approximately 0.5. To examine whether a single presynaptic neuron could control neuronal output (Woodruff and Sah, 2007), I induced a presynaptic neuron firing 10 ms prior to the postsynaptic current injection (Fig. 14C, D). As exemplified here, a strong depressing synapse profoundly suppressed the initial spike generation (spike probability, 0.58 ± 0.03 without presynaptic spikes vs. 0.34 ± 0.02 with presynaptic spikes, $n = 6$; $p < 0.05$, Wilcoxon signed-rank test; Fig. 14E). By contrast, there was no changes in neurons with a weak non-depressing synapse (spike probability, 0.55 ± 0.03 without presynaptic spikes vs. 0.48 ± 0.04 with presynaptic spikes, $n = 5$; $p = 0.13$, Wilcoxon signed-rank test; Fig. 14F). Because strong synapses markedly depressed during a 20-Hz train, firing by a single presynaptic neuron thus had little effect on subsequent postsynaptic spikes. In contrast, weak synapses led to a small reduction in the fifth AP probability (Fig. 14F). In line with the observations, the initial

IPSGs of strong synapses ($IPSG_1$: 2.2 ± 0.2 nS, n = 6; Fig. 14G) were significantly greater than those of weak synapses ($IPSG_1$: 0.5 ± 0.1 nS, n = 5; Fig. 14H; $p < 0.01$, Wilcoxon rank-sum test) but rapidly declined during the train (Fig. 14G, H). Taken together, distinct synaptic dynamics observed here indeed exerts a differential entrainment of spike activity in CeL neurons.

4. Conclusion

The CeL is a GABAergic core in the amygdala that is critical for the fear circuits, but the local circuit organization of the CeL is still unknown. The CeL neurons contain different functional and molecular features with unclear electrical properties. In this study, I first addressed the electrical properties of CeL neurons and found that there are two major electrically distinct populations, LS and ES cells, with distinct composition of Kv1 channels and displaying distinct autaptic transmission. Moreover, I investigate the functional connection of CeL GABAergic synapse (Fig. 15A). Analysis of the unitary GABAergic transmission revealed that the presynaptic cell type can determine the functional properties of autapses and CB_1R-mediated modulation of synaptic transmission between CeL neurons. In addition, pre- versus postsynaptic cell classes dictate the connectivity, efficacy, and dynamics of GABAergic synapses

between any two neurons (Fig. 15B). This wiring specificity and synaptic diversity have a great impact on the computational output in amygdala inhibitory networks.

Chapter 3 | Discussion

1. Significance of this study

In this study, using acute mouse amygdala slices, I found that the synapses formed by CeL neurons exhibit distinct STP with differential functional consequences. First, approximately 15% of CeL neurons form cell type-dependent functional autapses. Only autapses detected in ES cells contribute to enhancement of spike-timing precision. Second, CeL neurons form mutual connections with variable connection rates (approximately 10% on average) and preferentially target neurons of different classes. Third, the synaptic weight and the dynamics of STP are highly predictable from the identities of both presynaptic and postsynaptic neurons. Finally, I demonstrate that such wiring specificity and synaptic diversity have a great impact on neuronal activity in amygdala inhibitory networks.

2. A lack of correlation between intrinsic excitability and the neurochemical

marker SOM

The CeL neurons express cell subtype-specific neuropeptides SOM and PKC-δ (Cassell et al., 1986; Haubensak et al., 2010; Li et al., 2013; Penzo et al., 2014). Notably, SOM^+ and PKC-δ^+ neurons are largely nonoverlapping (Li et al., 2013). SOM^+ neurons display heterogeneous intrinsic excitability (Li et al., 2013). Among SOM^+ cells, 40% are LS cells while 60% are regular spiking (RS) cells (Haubensak et al., 2010; Li et al., 2013), which are similar to ES cells described in the present study. By contrast, the intrinsic excitability of PKC-δ^+ neurons is relatively homogeneous. Among PKC-δ^+ neurons, 86% are LS cells while 14% are RS cells (Haubensak et al., 2010). We also identified SOM^+ neurons, which readily express the red fluorescent protein tdTomato in the *Som-IRES-cre;Ai14* mice and found that 50% (22 of 44 cells) of SOM^+ neurons are ES cells (Fig. 13B), as a previous study also showed (Li et al., 2013), whereas 55% (12 of 22 cells) of SOM^- neurons are LS cells. Taken together, expression of molecular markers SOM and PKC-δ does not correlate with intrinsic excitability of the CeL neurons.

3. Possible mechanisms for cell type-specific STP

Presynaptic, postsynaptic, or other mechanisms could underlie STP (for reviews, see Zucker and Regehr, 2002; Fioravante and Regehr, 2011; Blackman et al., 2013). Several factors that regulate the size and dynamics of the presynaptic Ca^{2+} transient could potentially contribute to presynaptic mechanisms (Kamiya and Zucker, 1994; Koester and Sakmann, 2000; Rozov et al., 2001; Blatow et al., 2003; Koester and Johnston, 2005; Eggermann et al., 2011; Scimemi and Diamond, 2012; Catterall et al., 2013; Vyleta and Jonas, 2014; Liu et al., 2014). STP can also be achieved directly by postsynaptic mechanisms, e.g., receptor desensitization (Rozov and Burnashev, 1999), synapse location (Williams and Stuart, 2002), and biophysics of dendritic compartment (Abrahamsson et al., 2012). Notably, postsynaptic molecules or retrograde diffusible messengers from postsynaptic neurons can specifically regulate presynaptic partners and thus contribute to target-cell specific STP (Sylwestrak and Ghosh, 2012; see review by Blackman et al., 2013). In the present study, the finding in divergent connections reveals target-cell dependency (Fig. 11A). However, the result of convergent connections (Fig. 11B) strongly indicates that postsynaptic neurons alone do not solely determine the type of synapse (Gupta et al., 2000; Planert et al., 2010; Liu et al., 2014). Taken together, a precise match of pre- versus postsynaptic cell identities determines

STP, suggesting the existence of reciprocal interactions between presynaptic cells and postsynaptic partners (de Wit and Ghosh, 2016).

4. Nonrandom local circuits in the CeL

The connectivity between the CeL cells reveals non-uniform selectivity. The CeL cells prefer to form functional synapses with electrically distinct cell classes, whereas electrically identical cells have lower possibility to connect with each other. Our recent study (Liu et al., 2014) demonstrated that the connectivity of non-fast-spiking interneurons onto different target cell types in the hippocampal dentate gyrus is target-cell-type specific, whereas the fast-spiking interneurons innervate the different target cell types with similar probability. The hippocampal hilar local circuit also shows synapse selectivity. Approximately 88% of the intralamellar connection by hilar mossy cells targeting to the hilar interneurons (Larimer and Strowbridge, 2008). On the other hand, the interneurons in the hilus preferentially project to hilar mossy cells (Larimer and Strowbridge, 2008).

A key feature of nonrandom local circuits is cell-type-specific STP. Glutamatergic transmission in the neocortex displays target-cell-specific STP

(Markram et al., 1998; Reyes et al., 1998; see review by Blackman et al., 2013). In contrast, presynaptic cell subtype alone is sufficient to determine STP of inhibitory-to-inhibitory synapses in local circuits of different brain areas (Geracitano et al., 2007; Ma et al., 2012; Savanthrapadian et al., 2014). In this study, the rule governing STP of inhibitory synapses in the CeL is quite different. By recording the divergent and convergent connections, I found that the same GABAergic axon forms distinct types of synapses onto different classes of target neurons, whereas the postsynaptic neuron type alone cannot dictate the type of synapse (Fig. 11A, B). Similar to our study, Gupta et al. (2000) also demonstrated that the type of synapse formed is specific to both pre- and postsynaptic cell classes, which are distinguished by their anatomical and electrophysiological properties. Taken together, our findings support the notion that properly determining neuronal class is therefore critical when investigating synapse-specific STP.

5. The functional roles of the CeL autapse

In this study, I showed that only a small population (15%) of CeL neurons exhibited self-regulating GABAergic autaptic transmission. The most understand role of the autapses is the phase-lock ability. The phase-lock ability of spiking during

oscillatory fluctuations is thought to encode information, such as odor concentration in the olfactory bulb (Cang and Isaacson 2003) and animal location in hippocampal place cells (O'Keefe and Recce 1993).

The previous study demonstrated that significant contribution of autapses to the spike timing precision in the neocortical FS interneurons (Bacci and Huguenard, 2006). In the CeL autapses, although the increase of spike jitter cannot be fully explained by the aIPSG with the increment of the AP number. It is noted that, after the application of $GABA_A$ blocker, the jitter pattern changed as the effect of the removal of the autaptic conductance (Fig. 7D, G, H).

6. The possible mechanisms of the spike jitter regulation of CeL neurons

One possible mechanism regulating the spike timing precision in CeL cells might be GABAergic autaptic transmission. After each spike, the autaptic response is generated, which transiently decreases the probability of the following spike (Bacci et al., 2003a) and can thus regulate the timing or jitters of action potentials during the

sustained depolarization or input trains. The application of gabazine will block both autaptic transmission and spontaneous inhibition response (Bacci et al., 2003b). In addition, gabazine might block a tonic GABAergic membrane conductance (Stell and Mody, 2002; Semyanov et al., 2004; Farrant and Nusser, 2005) and might therefore influence spike jitters in CeL interneurons which is GABAergic autaptic transmission independent.

In my results, the jitter change of autapse-containing CeL cells are positive correlated with the strength of the autaptic conductance (Fig. 7E-H). Moreover, the pattern of the jitter change is similar with the short term plasticity of the CeL autapses. In addition, the spontaneous IPSPs on the spike jitter cannot be excluded using this approach. Further investigation still need to dissect the effect of the aIPSG and other inhibitory conductance using the dynamic clamp method (Lien et al., 2003).

Another possibility might due to the difference of the intrinsic excitability between the LS and ES cells. Since the LS cells contained I_D currents (Fig 4), the spike jitters during a step of depolarization might also be modulated by the composition of the voltage-gated ion channels and passive conductance, not solely depend on the aIPSG. Further studies still need to figure out the detail possible mechanisms of

intrinsic properties on the spike jitter of the CeL cells.

7. Role of the eCB signaling modulation in the CeA

Previous pharmacological experiments that application CB_1R antagonists to specific brain regions revealed that eCB signaling in the BLA and CeA are important for different phases of fear extinction. CB_1R blockade in the BLA led to an impairment of long-term extinction, whereas CB_1R antagonism in the CeA reduced within-session fear extinction (Kamprath et al., 2011). In addition, it was reported that the magnitude of depolarization-induced suppression of excitation (DSE) and DSI in the CeA was increased on the day after fear conditioning, showing that CB1R-mediated synaptic plasticity in the CeA is a consequence of fear conditioning. Pharmacological blockade of CB_1R in the infralimbic cortex would also impair the fear extinction (Kamprath et al., 2011).

On the other hand, a recent study revealed that the activity of PKC-δ^+ CeL neurons is highly associated with aversive behaviors and controls the appetite or food intake (Cai et al., 2014). Since the CeL PKC-δ^+ neurons received inhibitory local inputs, it is possible that the eCB signaling will participate in the regulation of the balance of

the CeL neuronal activity on either short-term or long-term excitatory/inhibitory balance and thus control state of the appetite-related behavior (Cai et al., 2014; Remikie et al., 2014).

8. Relevance of synaptic diversity to the information processing and storage

Previous study has demonstrated that the BLA inhibitory synapses formed by the presynaptic PV^+ neurons are sufficient to reduce the spiking probability and delay the firing phase of the BLA principal neurons (Woodruff and Sah, 2007). In the current study, I showed that variability of the synapses in the CeL can prevent action potentials in postsynaptic neurons in distinct temporal patterns. Furthermore, the unitary conductance of the short term depressing CeL synapses are enough to reduce the firing of the target cell in the early phase during the intense activity trains. In contrast, the non-depressing synapses have relatively small conductance but still can influence the late phase activity by the effect of the temporal summation.

The synaptic effect of GABA-mediated inhibitory neurotransmission can sculpt the activity of target neurons. Feedforward inhibition enhances spike-timing precision of cortical neurons by shortening the time window of excitatory postsynaptic

potential summation (Pouille and Scanziani, 2001). In contrast, feedback inhibition scales GABAergic inhibition to local excitatory output, thereby contributing to the generation of rhythmic activities (Mann et al., 2005). Based on microcircuit structures, the CeL comprises both feedforward and feedback inhibitory loops. Indeed, aIPSG effectively enhance the precision timing of early spikes in a train in ES cells. The degree of jitter in ES cells positively correlates with the autaptic inhibitory conductance. Furthermore, chemical synapses between CeL neurons differentially sculpt the activity pattern in these neurons. Although the specific functional purposes of this arrangement remain unknown, I propose that such combinatorial interactions between two CeL neurons can maximize synaptic diversity and may be relevant to synaptic modifications during learning and dynamic modulation of neuronal synchrony.

Experimental and theoretical studies suggest that minimum requirements for neuronal synchrony include mutually connected inhibitory interneurons, a time constant provided by $GABA_A$ receptors, and sufficient drive to induce spiking in the interneurons (Wang and Rinzel, 1992; Wang and Buzsáki, 1996; Bartos et al., 2001, 2002; Woodruff and Sah, 2007). Hu et al. (2011) has demonstrated that different types of inhibitory interneurons in the mouse barrel cortex are capable of coordinating their firing on a submillisecond timescale when paired with either same- or different-subtype

interneurons. Furthermore, the degree of neuronal synchrony correlates with inhibitory coupling strength (Bartos et al., 2002; Hu et al., 2011). Thus, inhibitory coupling via $GABA_A$ receptors between CeL neurons can contribute to the synchrony of CeL neurons *in vivo*. In this regard, modulation of CeL neuron activity or synaptic strength by various neuromodulators can fine-tune the synchrony of CeL neurons and thus control the CeL output (Viviani et al., 2011; Knobloch et al., 2012; Penzo et al., 2014). Overall, the STP between CeL neurons in local circuits is important in entrainment of their spike output to downstream CeM and other brainstem nuclei. Thus, further investigation into the functional significance of the specific connectivity pattern formed by CeL cells is critical for understanding the amygdala computation.

Figures and Tables

Figures

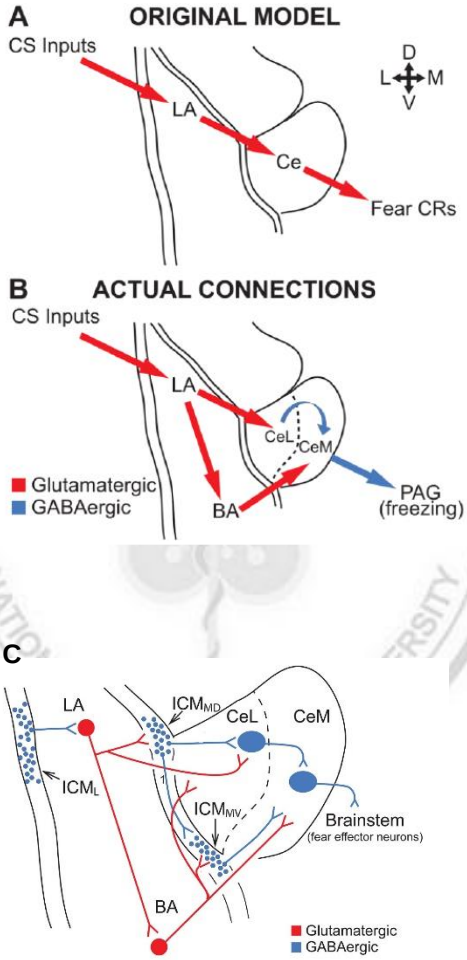

Figure 1. Intra-amygdala network involved in the fear processing (modified from Ducarci and Pare, 2012; Pare and Duvarci, 2014).

(A) Original model of the fear information processing within the amygdala proposed in the early 90's. The simplified model revealed the direct projections from the LA to the CeA output neurons.

(B) Revised model of the fear information processing within the amygdala indicated that other amygdala nuclei, (including the BA, ICM, and the CeL) can potentially pass the information between LA and CeM.

(C) Scheme of coronal section of the amygdala reveals the confirmed the intra- or inter-nucleus connections.

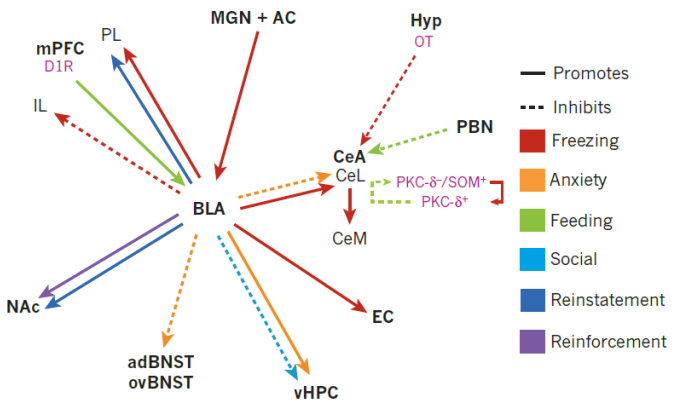

Figure 2. Amygdala circuits that are related to different emotional behavior domains (modified from Janak and Tye, 2015).

The diagram reveals projection-specific effects by either the optogenetic or chemogenetic manipulation of the intra- and inter-amygdala network connections on the behavioral consequences. The solid or dotted lines indicate the promotion or inhibition of the behaviors, respectively.

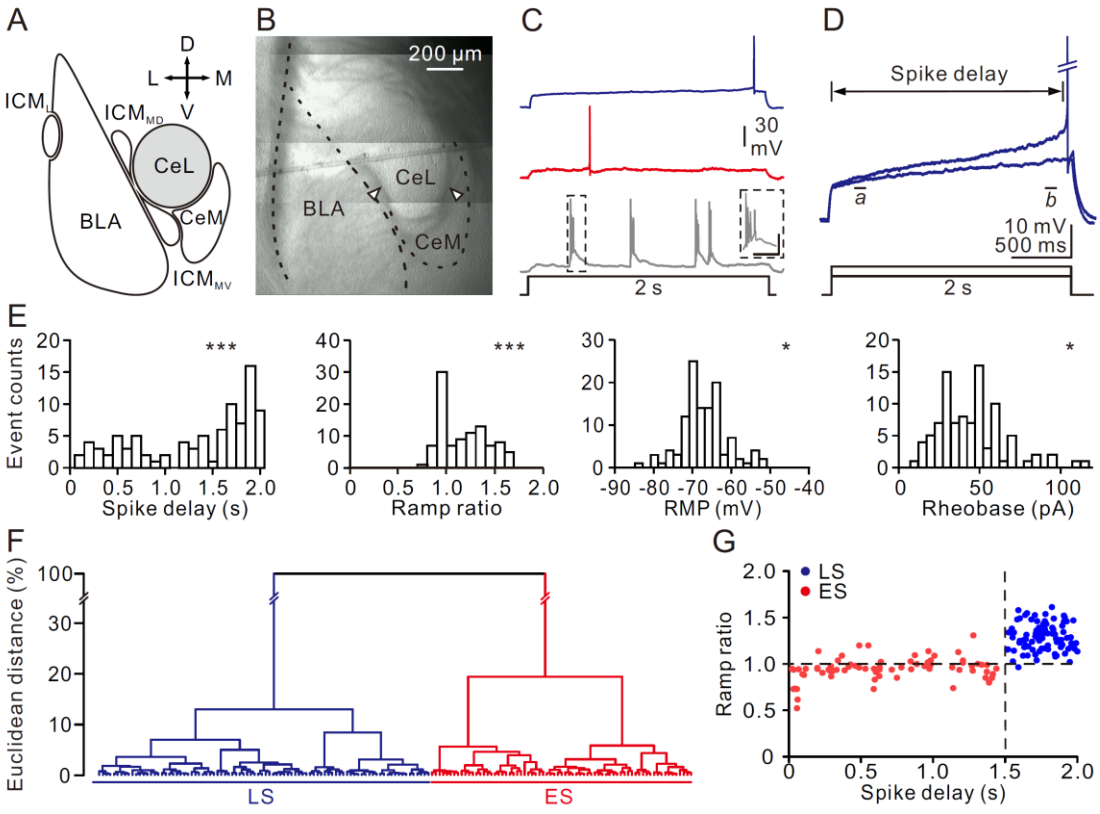

Figure 3. Heterogeneous intrinsic excitability of CeL neurons.

(A) Schematic drawing of the amygdala complex. Gray area denotes the recording area CeL. Axis: L, lateral; V, ventral; M, medial; D, dorsal.

(B) IR-DIC image of the amygdala complex from a coronal section of mouse brain. White arrowheads indicate the axon bundles. The borders of CeL, CeM, and BLA are outlined.

(C) Exemplar firing patterns recorded from LS (top), ES (middle), and LTB (bottom) cells. Inset: enlarged bursts (calibration: 15 ms, 30 mV). Notice that only 3.5% of recorded cells are LTB cells.

(D) Representative membrane responses of an LS cell to the supra- and subthreshold current injections. Note the slow depolarizing ramp. Bars *a* and *b* indicate how the average membrane potentials were measured for the calculation of ramp ratio (*b*/*a*). AP was truncated for display purposes.

(E) Histogram of spike delays, ramp ratios, RMPs, and rheobases from non-LTB cells. The p values from the D'Agostino-Pearson omnibus normality test demonstrate that the properties presented are not unimodally distributed. Asterisks indicate significant deviation from a normal distribution (*$p < 0.05$, **$p < 0.01$).

(F) Hierarchical cluster analysis of non-LTB neurons performed with electrophysiological parameters shown in (E) as the parameters for classification. The x-axis of the dendrogram represents the individual cells, and the y-axis represents the rescaled distance (squared Euclidean) between groups. Distinct types of neurons are marked with bars below the dendrogram.

(G) Scatterplot of spike delay vs. ramp ratio. Cells classified as LS and ES phenotypes in the dendrogram are blue and red, respectively. The dotted lines indicate the arbitrary cutoff values (spike delay of 1.5 s; ramp ratio of 1.0) that best separate the two populations shown in (F).

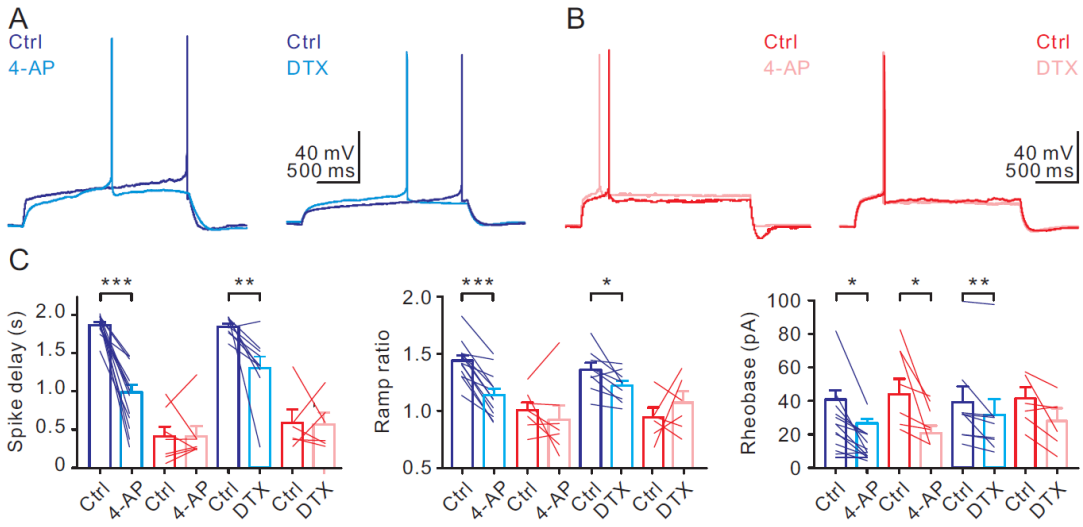

Figure 4. CeL neurons with different excitability showed differential sensitivity to K^+ channel blockers.

(A) Firing patterns of representative LS cells in control (Ctrl, blue) and in the presence of 30 μM 4-AP (left, light blue) or 100 nM DTX (right, light blue). Note the significant decreases in spike delay.

(B) Firing patterns of representative ES cells in Ctrl (red) and in the presence of 30 μM 4-AP (left, light red) or 100 nM DTX (right, light red).

(C) Summary of spike delay, ramp ratio, and rheobase before and after 4-AP or DTX application. Solid lines connected data obtained from the same cell. *$p < 0.05$, **$p < 0.01$, ***$p < 0.001$.

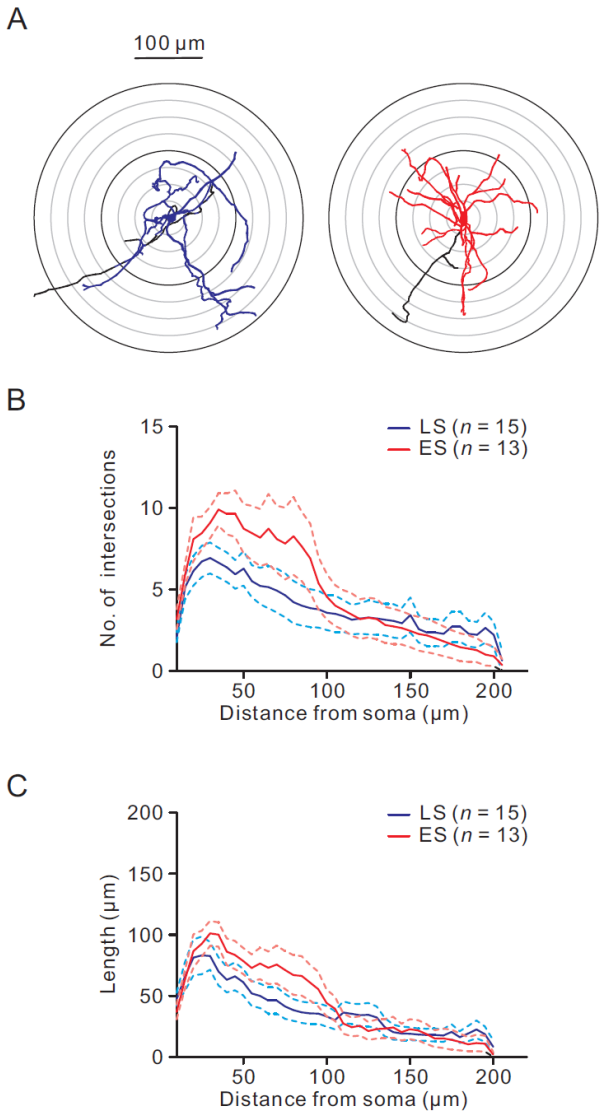

Figure 5. LS and ES cells had similar anatomical structures.

(A) Examples of anatomical reconstructions of biocytin-filled LS (blue) and ES (red) cells. Soma and dendrites of the LS cell are drawn in blue. Soma and dendrites of the ES cell are drawn in red. Putative axons of the LS and ES cells are drawn in black.

(B) Sholl analysis of the number of dendritic intersections against the distance from soma.

(C) Plot of dendritic length against the distance from soma. Solid and dashed lines indicate the average and SEM, respectively.

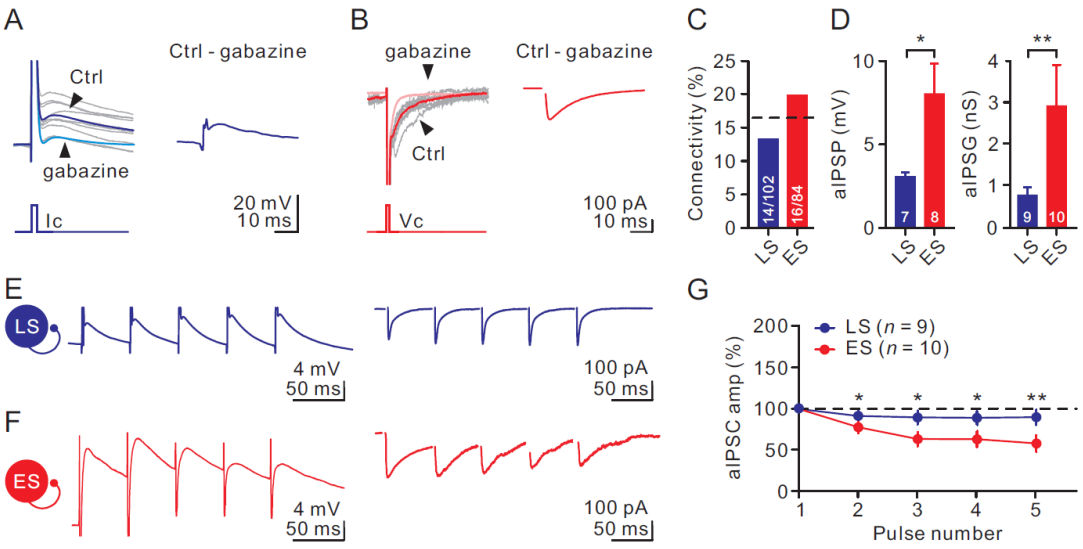

Figure 6. LS and ES cells displayed functionally distinct autaptic transmission.

(A) Left, APs (truncated for display purpose) evoked in an LS cell were followed by depolarization ($[Cl^-]_i$ = 144 mM), which was blocked by gabazine (1 μM). Average traces (blue) were recorded before and after addition of gabazine; 10 overlaid individual sweeps (gray) were recorded in Ctrl. Right, average autaptic IPSP (aIPSP) was obtained by digital subtraction of the average of 30 sweeps in the presence of gabazine from the average of 30 sweeps in Ctrl.

(B) Left, voltage steps to +20 mV from a holding potential of –70 mV in an ES cell elicited fast inward Na^+ current (truncated), followed by slower inward currents blocked by gabazine. Average traces (red) in Ctrl and in the presence of gabazine, respectively; individual sweeps (gray) recorded in Ctrl. Right, trace resulting after subtracting the gabazine-average trace (from 30 sweeps) from the Ctrl average trace (from 30 sweeps).

(C) Bar graph of autaptic connectivity. The horizontal dashed line indicates the average connectivity in any type of CeL autapse.

(D) Summary of autaptic IPSP amplitude (left) and autaptic conductance (right) in LS and ES cells. *$p < 0.05$, ** $p < 0.01$.

(E) A train of 5 aIPSPs (left; Ic, –70 mV, average of 30 sweeps) and aIPSCs (right; Vc, –70 mV, average of 30 sweeps) evoked at 20 Hz were recorded from LS cells; traces were isolated by gabazine.

(F) A train of 5 aIPSPs (left, average of 30 sweeps) and aIPSCs (right, average of 30 sweeps) recorded from ES cells; the same protocol and recording configuration as in (E).

(G) Plot of aIPSC amplitude (normalized to the first aIPSC in the same train) versus pulse number for each type of connections. The dashed line indicates a ratio of 1. * $p < 0.05$, ** $p < 0.01$.

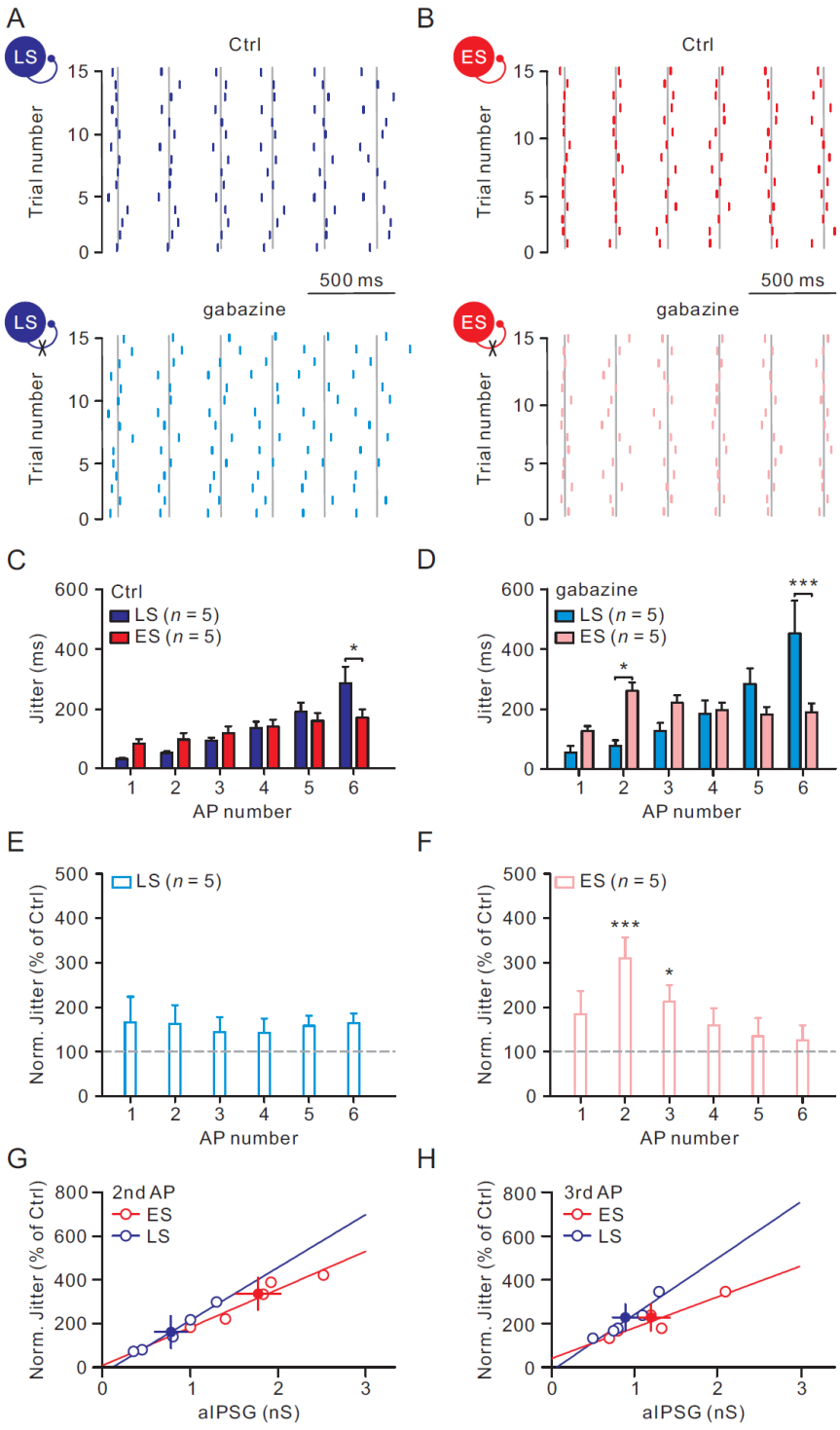

Figure 7. Selective enhancement of spike-timing precision by autaptic

transmission in ES cells.

(A–B) Top, raster plots of firing of LS (A, blue) and ES (B, red) neurons in response to 15 identical suprathreshold current injections (2 s, 10 – 20 pA). The gray line marks the average timing of each spike. Bottom, raster plots of the same neurons after gabazine application.

(C–D) Plot of spike jitter against AP number of both LS and ES autapses-containing cells before and after gabazine application.

(E–F) Plot of normalized jitter against spike number in LS (n = 5) and ES (n = 5) cells. Note that jitters in ES cells at the second and third spikes in the train were significantly increased.

(G–H) Plot of normalized jitters of the second (G) and third (H) spike against aIPSG. Curves represent linear fits to open circles. Filled circles are averages. * $p < 0.05$; *** $p < 0.001$.

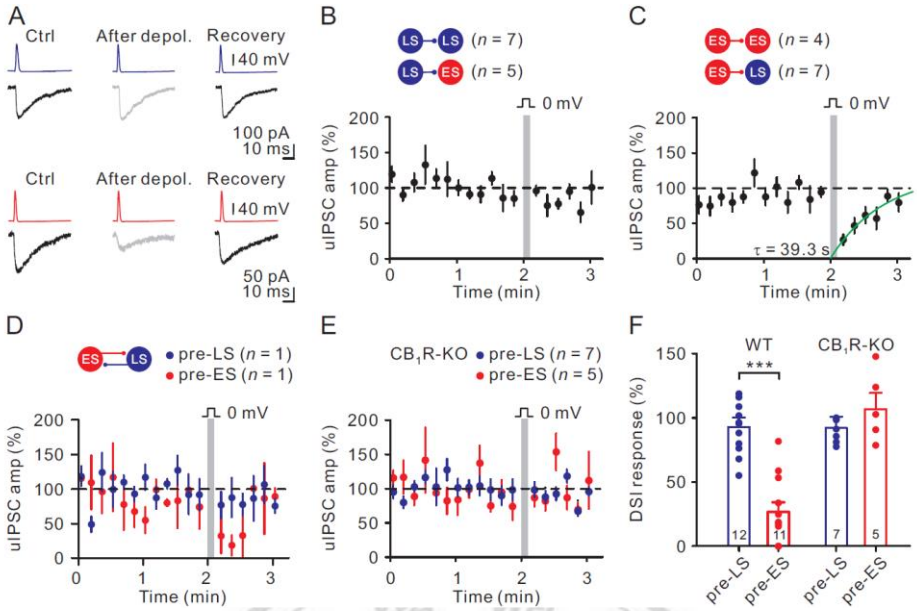

Figure 8. Presynaptic ES cell-specific depolarization-induced DSI.

(A) Top, representative uIPSC traces in Ctrl, after depolarization, and recovery from DSI of the CeL synapses in which the presynaptic phenotype is LS. To induce the DSI, postsynaptic cells were depolarized to 0 mV from –70 mV under Vc for 10 s. Bottom, representative uIPSC traces of the CeL synapses in which the presynaptic phenotype is ES.

(B) Summary of the uIPSC versus time from LS→LS (n = 7) or LS→ES (n = 5) pairs, with the voltage command shown on the top side. The gray bar indicates the time of DSI induction.

(C) Summary of the uIPSC versus time from ES→ES (n = 4) or ES→LS (n = 7) pairs. The recovery time course is fitted with a single exponential function.

(D) An example of reciprocally connected ES and LS neurons, revealing that DSI is specific to presynaptic ES cells.

(E) The lack of DSI in CB_1R knockout mice.

(F) Summary of DSI responses (average uIPSCs from 0 to 10 s right after the DSI protocol was normalized to baseline uIPSCs) of pairs with presynaptic-LS cell (n = 12) and presynaptic-ES cell (n = 11) in wild-type mice (WT) or in CB_1R knockout mice (CB_1R-KO) (presynaptic-LS cell, n = 7; presynaptic-ES cell, n = 5). *** $p < 0.001$.

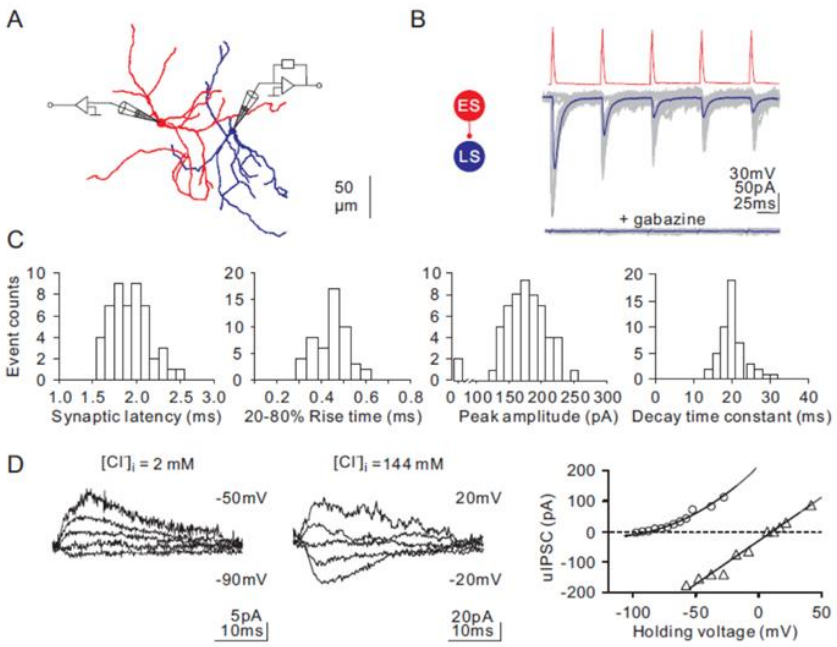

Figure 9. GABAergic neurotransmission between CeL neurons.

(A) Recording configuration and anatomical reconstructions of an example pair of CeL neurons. The presynaptic ES cell and postsynaptic LS cell are drawn in red and blue, respectively. Putative synapses are labeled by filled circles with the same color as the target LS cell dendrites.

(B) Schematic drawing illustrates the ES→LS connection. The same pair as shown in (A). APs in the presynaptic ES cell (top, red) elicited uIPSCs (middle, 50 superimposed sweeps in gray and averaged trace in blue) in a postsynaptic LS cell at -70 mV. Bottom traces were the averaged trace (blue) and 30 overlaid individual sweeps (gray) recorded in the presence of gabazine.

(C) Histograms of synaptic latencies, 20-80% rise times, decay time constants, and peak amplitudes of the first uIPSCs from the same pair.

(D) Traces of average uIPSCs in a pair at -90 to -50 mV (10 mV increment) with 2 mM $[Cl^-]_i$ (left); average uIPSCs in a pair at -20 to +20 mV with 144 mM $[Cl^-]_i$ (right). Plot of average uIPSCs vs. different holding potentials from pairs with different intracellular Cl^- concentrations. Data points of 2 and 144 mM $[Cl^-]_i$ are fitted with a polynomial function and a linear function, respectively. Semi-logarithmic plot of the E_{GABA} against $[Cl^-]_i$. The solid curve depicts the Goldman-Hodgkin-Katz voltage equation for the E_{GABA} plotted against $[Cl^-]_i$; the dashed line depicts the E_{GABA} plotted against $[Cl^-]_I$ for comparison when the relative permeability of HCO_3^- vs. Cl^- is zero.

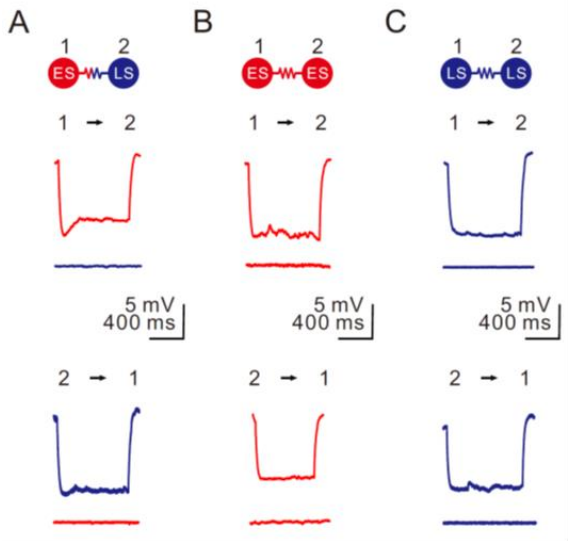

Figure 10. No electrical synapse between CeL neurons.

(A) An example of the gap junction test between the ES and LS cells. A -50pA, 1s hyperpolarization protocol was delivered to one of the simultaneously recorded ES and LS cell pairs, respectively. No membrane potential changes of the other cell were observed. Traces are average from 30 sweeps.

(B) An example of the gap junction test between two ES cells.

(C) An example of the gap junction test between two LS cells.

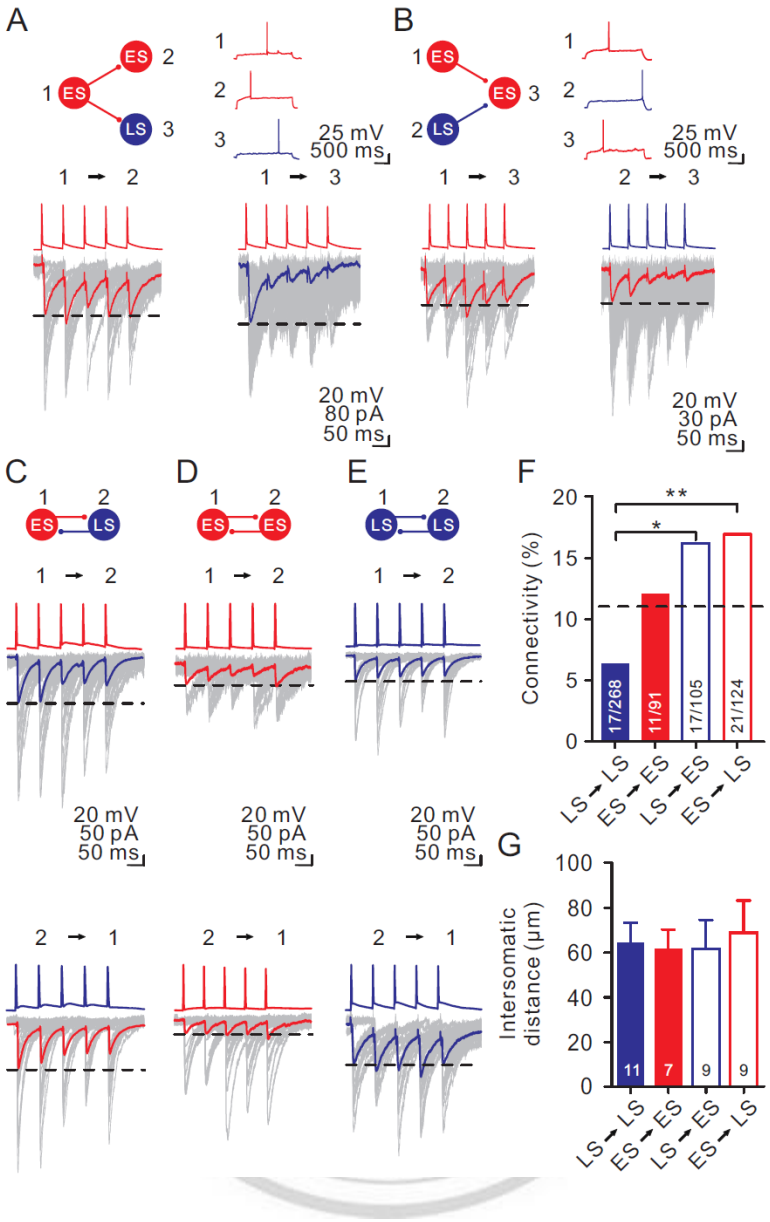

Figure 11. Specificity of GABAergic neurotransmission between CeL neurons.

(A) An example of divergent connections from an ES cell onto two distinct target cells. The presynaptic ES cell was stimulated by brief pulses of intracellular current injection. Simultaneous whole-cell voltage-clamp recordings of uIPSCs were made from an ES

and an LS cell. Representative firing patterns are shown. Average uIPSCs shown in bold traces superimposed on 30 example unitary responses (gray traces).

(B) An example of convergent connections from an ES cell and an LS cell onto a common target ES cell and their representative firing patterns. Average traces recorded from the ES→ES (left) and LS→ES (right) synapses are shown in bold traces superimposed on 30 example unitary responses (gray traces).

(C) An example of reciprocally connected ES and LS cells. Note that the ES→LS and LS→ES synapses showed similar short-term depression.

(D) An example of reciprocal connection between two ES cells. Note that ES #1→ES #2 and ES #2→ES #1 connections showed similar synaptic dynamics and little depression.

(E) An example of two reciprocally connected LS cells.

(F) Summary of the connectivity of CeL cells. The number of connections per number of attempts in each type of pair is indicated. The dashed line indicates the mean connectivity of any CeL neurons.

(G) Bar graph comparing intersomatic distance between chemically coupled neurons. Number of pairs is indicated. * $p < 0.05$; ** $p < 0.01$

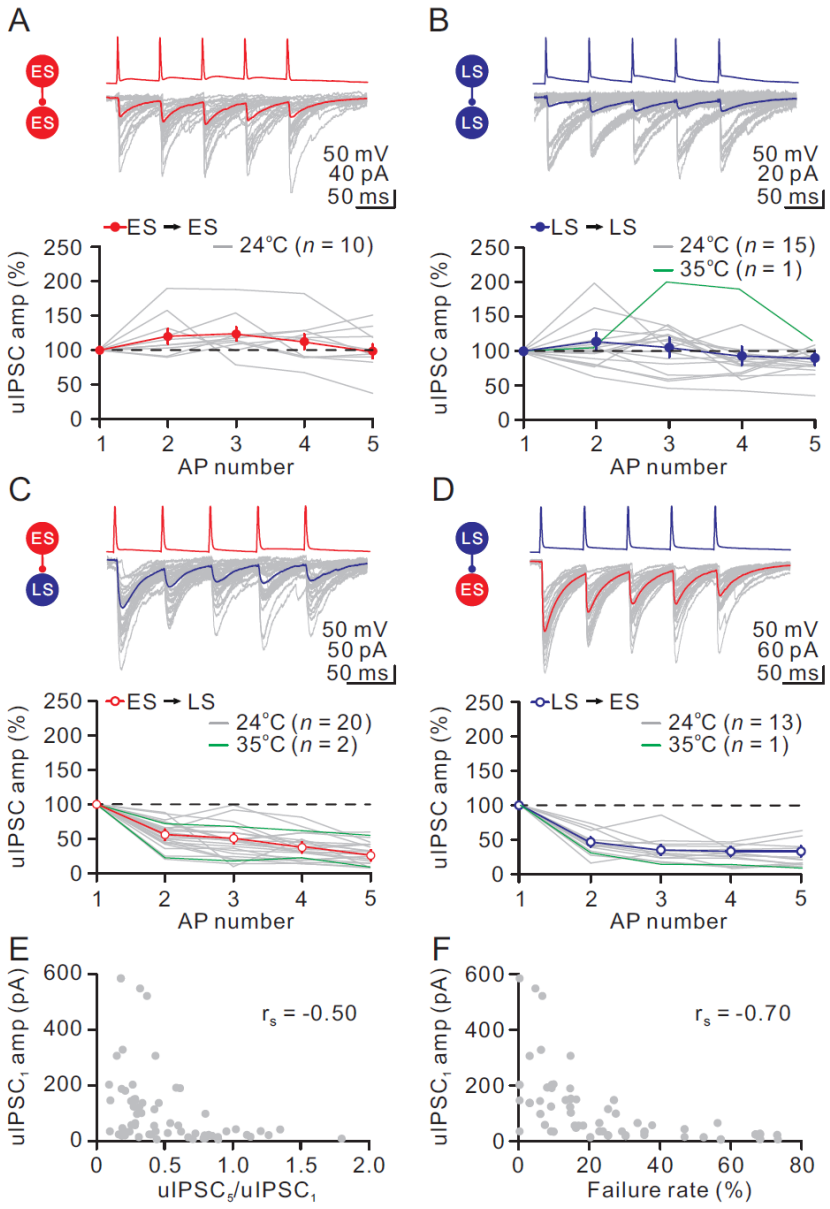

Figure 12. Pre- and postsynaptic cell type-specific STP.

(A–D) Representative records from unidirectionally connected ES→ES, LS→LS, ES →LS and LS→ES pairs. The presynaptic neurons were fired at 20 Hz (top trace); the bottom example traces show the averaged postsynaptic responses (from 50 single traces;

failures included) recorded at a holding potential of –70 mV ($[Cl^-]_i$ = 144 mM). Traces are color coded by subtype (ES, red; LS, blue). Graph, average amplitudes normalized to the amplitude of the first uIPSC ($uIPSC_1$) for each type of connections. Gray and green lines denote individual pairs recorded at 24 °C and 35 °C, respectively. The horizontal dotted lines indicate a ratio of 1.

(E) Plot of average $uIPSC_1$ amplitude against the amplitude ratio ($uIPSC_5/uIPSC_1$) for each type of connection.

(F) Plot of average $uIPSC_1$ amplitude against the failure rate of the $uIPSC_1$.

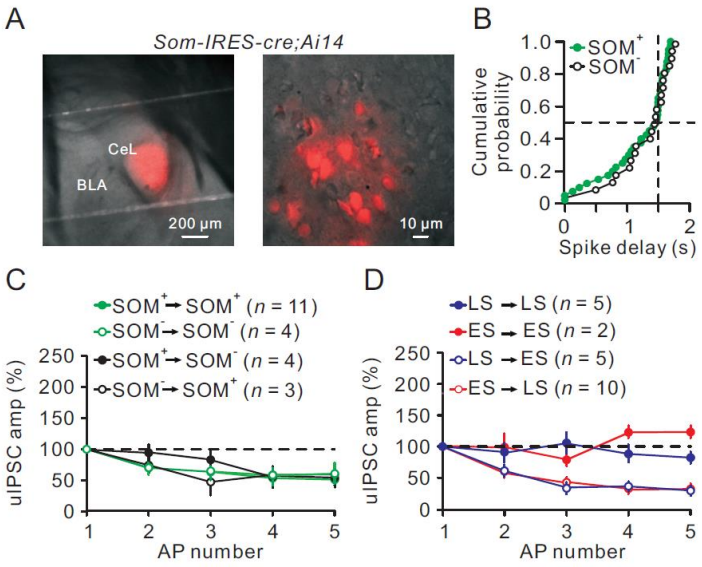

Figure 13. Cell type-specific transmission was independent of SOM expression in pre- and postsynaptic neurons.

(A) A section from the brain of an *Som-IRES-cre*;*Ai14* mouse. Left, The overlay of epifluorescence and IR-DIC images showing CeL with abundant red fluorescence. Right, enlargement of CeL; SOM^+ cells, which were visible (red) under epifluorescence.

(B) Cumulative distributions of spike delays from SOM^+ and SOM^- cells; the horizontal dashed line indicates the cumulative probability at 1.5 s spike delay in SOM^+ and SOM^- groups.

(C) Average amplitudes normalized to the amplitude of the $uIPSC_1$ for each type of connections using SOM as a cell type marker.

(D) Plot of normalized uIPSC amplitude versus AP number. Neurons in (C) and (D) are classified based on their firing patterns.

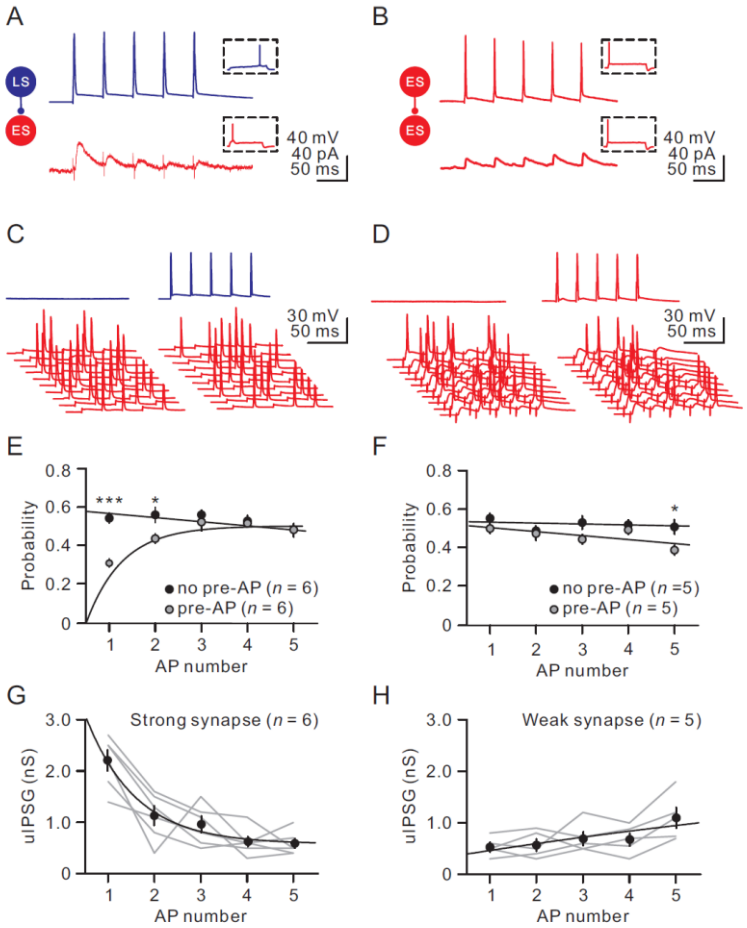

Figure 14. Cell type-specific STP differentially controlled neuronal output patterns.

(A–B) Example of synaptic transmission between electrically heterogeneous neurons (A) LS→ES or electrically homogeneous neurons (B) ES→ES. Representative firing patterns are shown in insets. A train of 5 APs at 20 Hz were elicited in the presynaptic

neurons at –70 mV in whole-cell current clamp (top traces); the bottom example traces show the averaged uIPSCs (from 30 single traces; failures included) recorded at a holding potential of –50 mV ($[Cl^-]_i$ = 7.5 mM and E_{Cl} = –75 mV). Traces are color coded by subtype (ES, red; LS, blue).

(C–D) Postsynaptic neurons were held at –50 mV and depolarized by brief current injections at 20 Hz (bottom traces). The firing probabilities were kept at approximately 0.5 by adjustment of current injection. A presynaptic neuron fired 10 ms prior to postsynaptic current injection.

(E–F) Plots show the comparison of spike probabilities of postsynaptic neurons (n = 6 for synapses between electrically heterogeneous neurons; n = 5 for electrically homogeneous neurons) in the presence or absence of coincident presynaptic neuron firing. * $p < 0.05$; *** $p < 0.001$.

(G–H) Plots of uIPSG versus AP number for strong and weak synapses. Gray lines denote individual pairs. Black lines and curves represent linear and exponential functions fitted to data points, respectively.

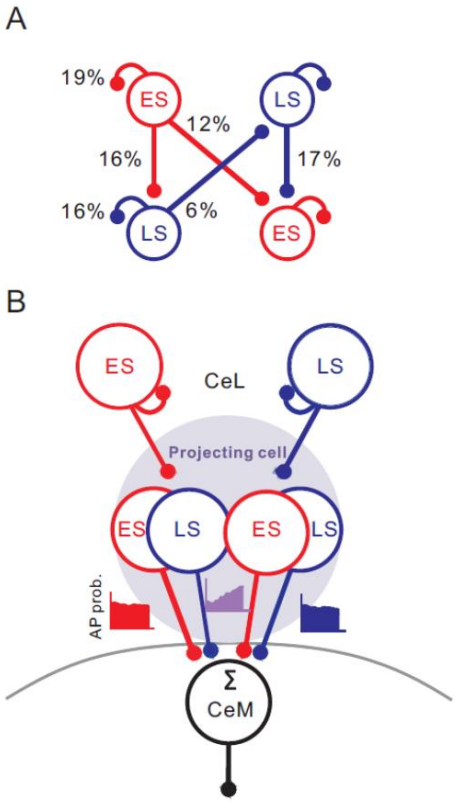

Figure 15. Summary of the connectivity of the CeL local circuit and the CeL neural output patterns sculpted by the cell-type specific STP.

(A) Schematic diagram of the CeL local network connectivity.

(B) Schematic diagram of the computational CeL output under the cell-type specific STP toward the downstream target CeM.

Tables

Table 1. Electrophysiological properties of LS versus ES cells in the CeL

	LS (105)	ES (80)	*p* value
RMP (mV)	–70.9 ± 0.5	–64.2 ± 0.8	< 0.0001
Rheobase (pA)	51.7 ± 2.0	38.9 ± 1.9	< 0.0001
Spike delay (ms)	1762 ± 23	626 ± 68	< 0.0001
Ramp ratio	1.29 ± 0.01	0.95 ± 0.01	< 0.0001
Input resistance (MΩ)	348 ± 10	350 ± 12	0.86
Membrane time constant (ms)	56.2 ± 5.3	55.4 ± 6.3	0.92
First AP threshold (mV)	–36.8 ± 0.4	–37.2 ± 0.5	0.81
First AP max. rising rate (V/s)	234 ± 8	226 ± 9	0.61
First AP max. falling rate (V/s)	42.8 ± 1.1	43.9 ± 1.3	0.44
First AP half-width (ms)	1.68 ± 0.01	1.58 ± 0.04	0.33
First AP height (mV)	89.3 ± 1.3	90.1 ± 1.2	0.45
Second AP max. rising rate (V/s)	203 ± 8	199 ± 12	0.51
Second AP max. falling rate (V/s)	42.3 ± 1.9	43.0 ± 2.8	0.36

Second AP height (mV)	80.2 ± 1.1	78.8 ± 1.3	0.96

Wilcoxon rank-sum test was performed to determine statistical significance between the groups. Numbers of cells are given in parentheses. All values are given as mean ± SEM.

Table 2. Properties of uIPSCs generated at GABAergic synapses

	Group 1 ES→ES (10)	Group 2 LS→LS (15)	Group 3 ES→LS (20)	Group 4 LS→ES (13)	ANOVA *p* value
$uIPSC_1$ latency (ms)	1.92 ± 0.21	1.95 ± 0.23	1.60 ± 0.13	1.80 ± 0.15	0.48
20–80% rise time (ms)	1.78 ± 0.12	1.61 ± 0.16	0.79 ± 0.05	0.90 ± 0.05	0.04[a]
$uIPSC_1$ decay τ (ms)	33.7 ± 3.9	28.7 ± 1.6	24.8 ± 2.9	20.8 ± 2.1	0.06
$uIPSC_1$ amplitude (pA)	34.2 ± 3.9	28.7 ± 5.2	177.2 ± 40.3	145.4 ± 47.1	0.0009[b]
Failure rate (%)	44 ± 5	40 ± 8	14 ± 3	16 ± 3	0.0002[c]
Paired-pulse ratio	1.21 ± 0.11	1.08 ± 0.08	0.57 ± 0.04	0.48 ± 0.04	< 0.0001[d]
Multiple-pulse ratio	1.02 ± 0.10	0.87 ± 0.05	0.29 ± 0.03	0.30 ± 0.04	< 0.0001[e]

$uIPSC_5CV/uIPSC_1CV$	0.88 ± 0.10	0.73 ± 0.10	0.12 ± 0.03	0.14 ± 0.04	0.005[f]

Data shown here were obtained in the V-clamp configuration from 24 ± 2 °C. One-way ANOVA was performed to compare the means among groups. Numbers of cells are given in parentheses. All values are given as mean ± SEM. Paired-pulse ratio (failures included) was defined as the ratio of the $uIPSC_2$ amplitude to the $uIPSC_1$ amplitude; multiple-pulse ratio (failures included) as the ratio of the $uIPSC_5$ amplitude to the $uIPSC_1$ amplitude in the 20-Hz train. The CV (coefficient of variation) of $uIPSC_5$ was normalized to the CV of $uIPSC_1$.

[a] $p < 0.05$; group 3 < 1 by Tukey's *post hoc* test, $p = 0.0001$; group 4 < 1 by Tukey's *post hoc* test, $p < 0.0001$; group 3 < 2 by Tukey's *post hoc* test, $p < 0.01$; group 4 < 2, $p = 0.0001$ by Tukey's *post hoc* test; group 1 vs. 2, $p = 0.70$; group 3 vs. 4, $p = 0.86$.

[b] $p < 0.01$; group 3 > 1 by Tukey's *post hoc* test, $p = 0.024$; group 4 > 1 by Tukey's *post hoc* test, $p = 0.026$; group 3 > 2 by Tukey's *post hoc* test, $p = 0.010$; group 4 > 2 by Tukey's *post hoc* test, $p = 0.012$; group 1 vs. 2, $p = 1.00$; group 3 vs. 4, $p = 0.98$.

[c] $p < 0.01$; group 3 < 1 by Tukey's *post hoc* test, $p = 0.0027$; group 4 < 1 by Tukey's *post hoc* test, $p = 0.011$; group 3 < 2, $p = 0.0035$; group 4 < 2, $p = 0.011$; group 1 vs. 2, $p = 0.78$; group 3 vs. 4, $p = 0.999$.

[d] $p < 0.01$; group 3 < 1 by Tukey's *post hoc* test, $p < 0.0001$; group 4 < 1 by Tukey's *post hoc* test, $p < 0.0001$; group 3 < 2 by Tukey's *post hoc* test, $p < 0.0001$; group 4 < 2 by Tukey's *post hoc* test, $p < 0.0001$; group 1 vs. 2, $p = 0.53$; group 3 vs. 4, $p = 0.69$.

[e] $p < 0.01$; group 3 < 1 by Tukey's *post hoc* test, $p < 0.0001$; group 4 < 1 by Tukey's *post hoc* test, $p < 0.0001$; group 3 < 2 by Tukey's *post hoc* test, $p < 0.0001$; group 4 < 2 by Tukey's *post hoc* test, $p < 0.0001$; group 1 vs. 2, $p = 0.23$; group 3 vs. 4, $p = 1$.

[f] $p < 0.01$; group 3 < 1 by Tukey's *post hoc* test, $p = 0.0003$; group 4 < 1 by Tukey's *post hoc* test, $p = 0.013$; group 3 < 2, $p < 0.0001$; group 4 < 2, $p < 0.0001$; group 1 vs. 2, $p = 0.31$; group 3 vs. 4, $p = 0.99$.

References

Abrahamsson T, Cathala L, Matsui K, Shigemoto R, Digregorio DA (2012) Thin dendrites of cerebellar interneurons confer sublinear synaptic integration and a gradient of short-term plasticity. Neuron 73:1159-1172.

Amano T, Amir A, Goswami S, Paré D (2012) Morphology, PKCδ expression, and synaptic responsiveness of different types of rat central lateral amygdala neurons. J Neurophysiol 108:3196-3205.

Amano T, Unal CT, Paré D (2010) Synaptic correlates of fear extinction in the amygdala. Nat Neurosci 13:489-494.

Asede D, Bosch D, Lüthi A, Ferraguti F, Ehrlich I (2015) Sensory inputs to intercalated cells provide fear-learning modulated inhibition to the basolateral amygdala. Neuron 86: 541-554.

Bacci A, Huguenard JR, Prince DA (2003) Functional autaptic neurotransmission in fast-spiking interneurons: a novel form of feedback inhibition in the neocortex. J Neurosci 23:859-866.

Bacci A, Huguenard JR (2006) Enhancement of spike-timing precision by autaptic transmission in neocortical inhibitory interneurons. Neuron 49:119-130.

Bartos M, Vida I, Frotscher M, Geiger JR, Jonas P (2001) Rapid signaling at inhibitory synapses in a dentate gyrus interneuron network. J Neurosci 21:2687-2698.

Bartos M, Vida I, Frotscher M, Meyer A, Monyer H, Geiger JR, Jonas P (2002) Fast synaptic inhibition promotes synchronized gamma oscillations in hippocampal interneuron networks. Proc Natl Acad Sci U S A 99:13222-13227.

Bean BP (2007) The action potential in mammalian central neurons. Nat Rev Neurosci 8:451-465.

Blackman AV, Abrahamsson T, Costa RP, Lalanne T, Sjöström PJ (2013) Target-cell-specific short-term plasticity in local circuits. Front Synaptic Neurosci 5:11.

Blatow M, Caputi A, Burnashev N, Monyer H, Rozov A (2003) Ca^{2+} buffer saturation underlies paired pulse facilitation in calbindin-D28k-containing terminals. Neuron 38:79-88.

Böhm C, Peng Y, Maier N, Winterer J, Poulet JF, Geiger JR, Schmitz D. Zucker (2015) Functional diversity of subicular principal cells during hippocampal ripples. J Neurosci 40:13608-13618.

Buchanan KA, Blackman AV, Moreau AW, Elgar D, Costa RP, Lalanne T, Tudor Jones AA, Oyrer J, Sjöström PJ (2012) Target-specific expression of presynaptic NMDA receptors in neocortical microcircuits. Neuron 75:451-466.

Busti D, Geracitano R, Whittle N, Dalezios Y, Manko M, Kaufmann W, Satzler K, Singewald N, Capogna M, Ferraguti F. (2011) Different fear states engage distinct networks within the intercalated cell clusters of the amygdala. J Neurosci 31: 5131-5144.

Cador M, Robbins TW, Everitt BJ (1989) Involvement of the amygdala in stimulus reward associations: interaction with the ventral striatum. Neuroscience 30: 77-86.

Cai H, Haubensak W, Anthony TE, Anderson DJ (2014) Central amygdala PKC-δ(+) neurons mediate the influence of multiple anorexigenic signals. Nat Neurosci 17:1240-1248.

Campanac E, Gasselin C, Baude A, Rama S, Ankri N, Debanne D (2013) Enhanced intrinsic excitability in basket cells maintains excitatory-inhibitory balance in hippocampal circuits. Neuron 77:712-722.

Cassell MD, Freedman LJ, Shi C (1999) The intrinsic organization of the central extended amygdala. Ann N Y Acad Sci 877:217-241.

Cassell MD, Gray TS, Kiss JZ (1986) Neuronal architecture in the rat central nucleus of the amygdala: a cytological, hodological, and immunocytochemical study. J Comp Neurol 246:478-499.

Catterall WA, Leal K, Nanou E (2013) Calcium channels and short-term synaptic plasticity. J Biol Chem 288:10742-10749.

Cauli B, Porter JT, Tsuzuki K, Lambolez B, Rossier J, Quenet B, Audinat E (2000) Classification of fusiform neocortical interneurons based on unsupervised clustering. Proc Natl Acad Sci U S A 97:6144-6149.

Chiang PH, Chien TC, Chen CC, Yanagawa Y, Lien CC (2015) ASIC-dependent LTP at multiple glutamatergic synapses in amygdala network is required for fear memory. Sci Rep 5:10143.

Chieng BC, Christie MJ, Osborne PB (2006) Characterization of neurons in the rat central nucleus of the amygdala: cellular physiology, morphology, and opioid sensitivity. J Comp Neurol 497:910-927.

Ciocchi S, Herry C, Grenier F, Wolff SB, Letzkus JJ, Vlachos I, Ehrlich I, Sprengel R, Deisseroth K, Stadler MB, Müller C, Lüthi A (2010) Encoding of conditioned fear in central amygdala inhibitory circuits. Nature 468:277-282.

Connelly WM, Lees G (2010) Modulation and function of the autaptic connections of layer V fast spiking interneurons in the rat neocortex. J Physiol 588:2047-2063.

Cossart R, Petanjek Z, Dumitriu D, Hirsch JC, Ben-Ari Y, Esclapez M, Bernard C (2006) Interneurons targeting similar layers receive synaptic inputs with similar kinetics. Hippocampus 16:408-420.

de Wit J, Ghosh A (2016) Specification of synaptic connectivity by cell surface interactions. Nat Rev Neurosci 17:4.

Debanne D, Guérineau NC, Gähwiler BH, Thompson SM (1996) Paired-pulse facilitation and depression at unitary synapses in rat hippocampus: quantal fluctuation affects subsequent release. J Physiol 491:163-176.

Dodson PD, Barker MC, Forsythe ID (2002) Two heteromeric Kv1 potassium channels differentially regulate action potential firing. J Neurosci 22:6953-6961.

Duvarci S, Pare D (2014) Amygdala microcircuits controlling learned fear. Neuron 82:966-980.

Eggermann E, Bucurenciu I, Goswami SP, Jonas P (2011) Nanodomain coupling between Ca^{2+} channels and sensors of exocytosis at fast mammalian synapses. Nat Rev Neurosci 13:7-21.

Ehrlich I, Humeau Y, Grenier F, Ciocchi S, Herry C, Lüthi A (2009) Amygdala inhibitory circuits and the control of fear memory. Neuron 62:757-771.

Everitt BJ, Cador M, Robbins TW (1989) Interactions between the amygdala and ventral striatum in stimulus-reward associations: studies using a second-order schedule of sexual reinforcement. Neuroscience 30: 63-75.

Felix-Ortiz AC, Beyeler A, Seo C, Leppla CA, Wildes CP, Tye KM (2013) BLA to vHPC inputs modulate anxiety-related behaviors. Neuron 79: 658-664.

Felix-Ortiz AC, Tye KM (2014) Amygdala inputs to the ventral hippocampus bidirectionally modulate social behavior. J Neurosci 34: 586-595.

Fioravante D, Regehr WG (2011) Short-term forms of presynaptic plasticity. Curr Opin Neurobiol 21:269-274.

Geracitano R, Kaufmann WA, Szabo G, Ferraguti F, Capogna M (2007) Synaptic heterogeneity between mouse paracapsular intercalated neurons of the amygdala. J Physiol 585:117-134.

Goldberg EM, Clark BD, Zagha E, Nahmani M, Erisir A, Rudy B (2008) K^+ channels at the axon initial segment dampen near-threshold excitability of neocortical fast-spiking GABAergic interneurons. Neuron 58:387-400.

Graves AR, Moore SJ, Bloss EB, Mensh BD, Kath WL, Spruston N (2012) Hippocampal pyramidal neurons comprise two distinct cell types that are countermodulated by metabotropic receptors. Neuron 76:776-789.

Gupta A, Wang Y, Markram H (2000) Organizing principles for a diversity of GABAergic interneurons and synapses in the neocortex. Science 287:273-278.

Hall E (1972) The amygdala of the cat: A Golgi Study. Z Zellforsch 1972; 134: 439-458.

Han JH, Kushner SA, Yiu AP, Cole CJ, Matynia A, Brown RA, Neve RL, Guzowshi JF, Silva AJ,

Josselyn SA (2007) Neuronal competition and selection during memory formation. Science 316:457-460.

Haubensak W, Kunwar PS, Cai H, Ciocchi S, Wall NR, Ponnusamy R, Biag J, Dong HW, Deisseroth K, Callaway EM, Fanselow MS, Lüthi A, Anderson DJ (2010) Genetic dissection of an amygdala microcircuit that gates conditioned fear. Nature 468:270-276.

Hu H, Ma Y, Agmon A (2011) Submillisecond firing synchrony between different subtypes of cortical interneurons connected chemically but not electrically. J Neurosci 31:3351-3361.

Janak PH, Tye KM (2015) From circuits to behaviour in the amygdala. Nature 517: 284-292.

Jasnow AM, Ressler KJ, Hammack SE, Chhatwal JP, Rainnie DG (2009) Distinct subtypes of cholecystokinin (CCK)-containing interneurons of the basolateral amygdala identified using a CCK promoter-specific lentivirus. J Neurophysiol 101:1494-1506.

Johansen JP, Cain CK, Ostroff LE, LeDoux JE (2011) Molecular mechanisms of fear learning and memory. Cell 147:509-524.

Kamiya H, Zucker RS (1994) Residual Ca^{2+} and short-term synaptic plasticity. Nature 371:603-606.

Kamprath K, Romo-Parra H, Häring M, Gaburro S, Doengi M, Lutz B, Pape HC (2011) Short-term adaptation of conditioned fear responses through endocannabinoid signaling in the central amygdala. Neuropsychopharmacology 36: 652–663.

Killcross S, Robbins TW, Everitt BJ (1997) Different types of fear-conditioned behaviour mediated by separate nuclei within amygdala. Nature 388:377-380.

Kirchheim F, Tinnes S, Haas CA, Stegen M, Wolfart J (2013) Regulation of action potential delays via voltage-gated potassium Kv1.1 channels in dentate granule cells during hippocampal epilepsy. Front Cell Neurosci 7:248.

Knobloch HS, Charlet A, Hoffmann LC, Eliava M, Khrulev S, Cetin AH, Osten P, Schwarz MK, Seeburg PH, Stoop R, Grinevich V (2012) Evoked axonal oxytocin release in the central amygdala attenuates fear response. Neuron 73:553-566.

Koester HJ, Johnston D (2005) Target cell-dependent normalization of transmitter release at neocortical synapses. Science 308:863-866.

Koester HJ, Sakmann B (2000) Calcium dynamics associated with action potentials in single nerve terminals of pyramidal cells in layer 2/3 of the young rat neocortex. J Physiol 529:625-646.

Larimer P, Strowbridge BW (2008) Nonrandom local circuits in the dentate gyrus. J Neurosci 28:12212-12223.

LeDoux J (2007) The amygdala. Curr Biol 17:R868-874.

LeDoux J (2012) Rethinking the emotional brain. Neuron 73:653-676.

LeDoux JE, Iwata J, Cicchetti P, Reis DJ (1988) Different projections of the central amygdaloid nucleus mediate autonomic and behavioral correlates of conditioned fear. J Neurosci 8:2517-2529.

Li H, Penzo MA, Taniguchi H, Kopec CD, Huang ZJ, Li B (2013) Experience-dependent modification of a central amygdala fear circuit. Nat Neurosci 16:332-339.

Lien CC, Jonas P (2003) Kv3 potassium conductance is necessary and kinetically optimized for high-frequency action potential generation in hippocampal interneurons. J Neurosci 23:2058-2068.

Likhtik E, Popa D, Apergis-Schoute J, Fidacaro GA, Pare´ D (2008) Amygdala intercalated neurons are required for expression of fear extinction. Nature 454:642-645.

Liu YC, Cheng JK, Lien CC (2014) Rapid dynamic changes of dendritic inhibition in the dentate gyrus by presynaptic activity patterns. J Neurosci 4:1344-1357.

Lopez de Armentia M, Sah P (2004) Firing properties and connectivity of neurons in the rat lateral central nucleus of the amygdala. J Neurophysiol 92:1285-1294.

Ma Y, Hu H, Agmon A (2012) Short-term plasticity of unitary inhibitory-to-inhibitory synapses depends on the presynaptic interneuron subtype. J Neurosci 32:983-988.

Madisen L, Zwingman TA, Sunkin SM, Oh SW, Zariwala HA, Gu H, Ng LL, Palmiter RD, Hawrylycz MJ, Jones AR, Lein ES, Zeng H (2010) A robust and high-throughput Cre reporting and characterization system for the whole mouse brain. Nat Neurosci 1:133-140.

Mann E, Suckling J, Hájos N, Greenfield S, Paulsen O (2005) Perisomatic feedback inhibition underlies cholinergically induced fast network oscillations in the rat hippocampus in vitro. Neuron 45:105-117.

Maren S (2001) Neurobiology of Pavlovian fear conditioning. Annu Rev Neurosci 24:897-931.

Markram H, Wang Y, Tsodyks M (1998) Differential signaling via the same axon of neocortical pyramidal neurons. Proc Natl Acad Sci U S A 95:5323-5328.

Martina M, Royer S, Paré D (1999) Physiological properties of central medial and central lateral amygdala neurons. J Neurophysiol 82:1843-1854.

Martina M, Schultz JH, Ehmke H, Monyer H, Jonas P (1998) Functional and molecular differences between voltage-gated K^+ channels of fast-spiking interneurons and pyramidal neurons of rat hippocampus. J Neurosci 18:8111-8125.

Mathews PJ, Jercog PE, Rinzel J, Scott LL, Golding NL (2010) Control of submillisecond synaptic timing in binaural coincidence detectors by Kv1 channels. Nat Neurosci 13:601-609.

Myatt DR, Hadlington T, Ascoli GA, Nasuto SJ (2012) Neuromantic - from semi-manual to semi-automatic reconstruction of neuron morphology. Front Neuroinform 6:4.

Namburi P, Beyeler A, Yorozu S, Calhoon GG, Halbert SA, Wichmann R, Holden SS, Mertens KL, Anahtar M, Felix-Ortiz AC, Wickersham IR, Gray JM, Tye KM (2015) A circuit mechanism for differentiating positive and negative associations. Nature 520:675-678.

Palomares-Castillo E, Hernandez-Perez OR, Perez-Carrera D, Crespo-Ramırez M, Fuxe K, Perez de la Mora M. (2012). The intercalated paracapsular islands as a module for integration of signals regulating anxiety in the amygdala. Brain Res 1476: 211–234.

Pare D, Duvarci S (2012) Amygdala microcircuits mediating fear expression and extinction. Curr Opin Neurobiol 22:717-723.

Paré D, Quirk GJ, Ledoux JE (2004) New vistas on amygdala networks in conditioned fear. J Neurophysiol 92:1-9.

Penzo MA, Robert V, Li B (2014) Fear conditioning potentiates synaptic transmission onto long-range projection neurons in the lateral subdivision of central amygdala. J Neurosci 34:2432-2437.

Penzo, MA, Robert V, Tucciarone J, De Bundel D, Wang M, Van Aelst L, Darvas M, Parada LF, Palmiter RD, He M, Huang ZJ, Li B (2015) The paraventricular thalamus controls a central amygdala fear circuit. Nature 519: 455-459.

Pitkänen A, Savander V, LeDoux JE (1997) Organization of intra-amygdaloid circuitries in the rat: an emerging framework for understanding functions of the amygdala. Trends Neurosci 20:517-523.

Planert H, Szydlowski SN, Hjorth JJ, Grillner S, Silberberg G (2010) Dynamics of synaptic transmission between fast-spiking interneurons and striatal projection neurons of the direct and indirect pathways. J Neurosci 30:3499-3507.

Pouille F, Scanziani M (2001) Enforcement of temporal fidelity in pyramidal cells by somatic feed-forward inhibition. Science 293:1159-1163.

Ramikie TS, Nyilas R, Bluett RJ, Gamble-George JC, Hartley ND, Mackie K, Watanabe M, Katona I, Patel S (2014) Multiple mechanistically distinct modes of endocannabinoid mobilization at central amygdala glutamatergic synapses. Neuron 81:1111-1125.

Reyes A, Lujan R, Rozov A, Burnashev N, Somogyi P, Sakmann B (1998) Target-cell-specific facilitation and depression in neocortical circuits. Nat Neurosci 4:279-85.

Roberto M, Cruz M, Bajo M, Siggins GR, Parsons LH, Schweitzer P (2010) The endocannabinoid system tonically regulates inhibitory transmission and depresses the effect of ethanol in central amygdala. Neuropsychopharmacology 35:1962-1972.

Romanski LM, LeDoux JE (1993) Information cascade from primary auditory cortex to the amygdala: corticocortical and corticoamygdaloid projections of temporal cortex in the rat. Cereb Cortex 3:515–532.

Rozov A, Burnashev N, Sakmann B, Neher E (2001) Transmitter release modulation by intracellular Ca^{2+} buffers in facilitating and depressing nerve terminals of pyramidal cells in layer 2/3 of the rat neocortex indicates a target cell-specific difference in presynaptic calcium dynamics. J Physiol 531:807-826.

Rozov A, Burnashev N (1999) Polyamine-dependent facilitation of postsynaptic AMPA receptors counteracts paired-pulse depression. Nature 401:594-598.

Sah P, Faber ES, Lopez De Armentia M, Power J (2003) The amygdaloid complex: anatomy and physiology. Physiol Rev 83:803-834.

Savanthrapadian S, Meyer T, Elgueta C, Booker SA, Vida I, Bartos M (2014) Synaptic properties of SOM- and CCK-expressing cells in dentate gyrus interneuron networks. J Neurosci 34:8197-8209.

Scimemi A, Diamond JS (2012) The number and organization of Ca^{2+} channels in the active zone shapes neurotransmitter release from Schaffer collateral synapses. J Neurosci 32:18157-18176.

Sholl DA (1953) Dendritic organization in the neurons of the visual and motor cortices of the cat. J Anat 87:387-406.

Sigurdsson T, Doyère V, Cain CK, LeDoux JE (2007) Long-term potentiation in the amygdala: a cellular mechanism of fear learning and memory. Neuropharmacology 52:215-227.

Smith Y, Pare D (1994) Intra-amygdaloid projections of the lateral nucleus in the cat: PHA-L anterograde labeling combined with post-embedding GABA and glutamate immunocytochemistry. J Comp Neurol 342:232-248.

Sosulina L, Graebenitz S, Pape HC (2010) GABAergic interneurons in the mouse lateral amygdala: a classification study. J Neurophysiol 104:617-626.

Spearman C (1904) The proof and measurement of association between two things. Am J Psychol 15:72-101.

Storm JF (1988) Temporal integration by a slowly inactivating K^+ current in hippocampal neurons. Nature 336:379-381.

Sylwestrak EL, Ghosh A (2012) Elfn1 regulates target-specific release probability at CA1-interneuron synapses. Science 338:536-540.

Tamás G, Buhl EH, Somogyi P (1997) Massive autaptic self-innervation of GABAergic neurons in cat visual cortex. J Neurosci 17:6352-6364.

Taniguchi H, He M, Wu P, Kim S, Paik R, Sugino K, Kvitsani D, Fu Y, Lu J, Lin Y, Miyoshi G, Shima Y, Fishell G, Nelson SB, and Huang ZJ (2011) A resource of Cre driver lines for genetic targeting of GABAergic neurons in cerebral cortex. Neuron 71:995-1013.

Tye KM, Prakash R, Kim SY, Fenno LE, Grosenick L, Zarabi H, Thompson KR, Gradinaru V, Ramakrishnan C, Deisseroth K (2011) Amygdala circuitry mediating reversible and bidirectional control of anxiety. Nature 471: 358-362.

Viviani D, Charlet A, van den Burg E, Robinet C, Hurni N, Abatis M, Magara F, Stoop R (2011) Oxytocin selectively gates fear responses through distinct outputs from the central amygdala. Science 333:104-107.

Vyleta NP, Jonas P (2014) Loose coupling between Ca^{2+} channels and release sensors at a plastic hippocampal synapse. Science 343:665-670.

Walker GA (2002) Common statistical methods for clinical research with SAS® examples, second edition. Cary, NC: SAS Institute Inc.

Wang XJ, Buzsáki G (1996) Gamma oscillation by synaptic inhibition in a hippocampal interneuronal network model. J Neurosci 16:6402-6413.

Wang XJ, Rinzel J (1992) Alternating and synchronous rhythms in reciprocally inhibitory model neurons. Neural Comput 4:84-97.

Ward JH (1963) Hierarchical grouping to optimize an objective function. J Am Stat Assoc 58:236-244.

Wilensky AE, Schafe GE, Kristensen MP, LeDoux JE (2006) Rethinking the fear circuit: the central nucleus of the amygdala is required for the acquisition, consolidation, and expression of Pavlovian fear conditioning. J Neurosci 26:12387-12396.

Williams SR, Stuart GJ (2002) Dependence of EPSP efficacy on synapse location in neocortical pyramidal neurons. Science 295:1907-1910.

Wolff SB, Gründemann J, Tovote P, Krabbe S, Jacobson GA, Müller C, Herry C, Ehrlich I, Friedrich RW, Letzkus JJ, Lüthi A (2014) Amygdala interneuron subtypes control fear learning through disinhibition. Nature 509: 453-458.

Woodruff AR, Sah P (2007) Inhibition and synchronization of basal amygdala principal neuron spiking by parvalbumin-positive interneurons. J Neurophysiol 98:2956-2961.

Zimmer A, Zimmer AM, Hohmann AG, Herkenham M, Bonner TI (1999) Increased mortality, hypoactivity, and hypoalgesia in cannabinoid CB1 receptor knockout mice. Proc Natl Acad Sci U S A 96:5780-5785.

Zucker RS, Regehr WG (2002) Short-term synaptic plasticity. Annu Rev Physiol 64:355-405.

CURRICULUM VITAE

Wen-Hsien Hou, B.S.
National Yang-Ming University
Institute of Neuroscience
No. 155, Section 2, LiNong Street, Beitou District
Taipei City 112, Taiwan
Work: +886 (02) 2826-7000#6090; Fax: +886 (02) 2821-5307; E-mail: wanshanho@gmail.com

NAME	POSITION TITLE
Hou, Wen-Hsien	Ph.D. student of Neuroscience

EDUCATION/TRAINING

INSTITUTION AND LOCATION	DEGREE *(if applicable)*	YEAR(s)	FIELD OF STUDY
National Tsing Hua University, Taiwan	B.S.	2007-2011	Department of Life Science
National Yang-Ming University, Taiwan	Ph.D.	2011-present	Institute of Neuroscience

A. Personal statement.

Fear is a highly conserved emotional process among species. One of the key brain region that gates the output of fear and controls fear learning is the lateral subdivision of the central amygdala (CeL). The CeL, a small core that is composed of over 90% intermingled GABA (γ-aminobutyric acid)-ergic neurons, is considered to provide tonic inhibition to tune the downstream amygdala region. Although recently the CeL neurons has been functionally characterized as CeL_{on} or CeL_{off} neurons by the activity change after fear learning, the intrinsic properties and functional connectivity of the intra-CeL inhibitory microcircuit still remain unknown. In the past 5 years, I focused on the heterogeneity of CeL neurons and mapping the CeL GABAergic synapses by exploring the expression of functional marker (somatostatin), electrical properties, neurotransmissions, and the short-term plasticity of CeL synapses. I will further have insight into whether the CeL synapses would be modified during or after the fear conditioning test.

B. Position and Honors.

Other Experience and Professional Memberships

2013 – Present: Student Member, Neuroscience Society of Taiwan
2013 – 2014: Student Member, Society for Neuroscience (SfN), USA

Honors

2016 Excellent PhD Thesis Fellowship, National Yang-Ming University, Taiwan.
2013 Poster competition award, Neuroscience society of Taiwan.
2013 Accepted direct-promotion fellowship from institute of neuroscience, National Yang-Ming University, Taiwan.
2012 Poster competition award, National Yang-Ming University, Taiwan.
2009 Accepted summer research fellowship from the National Health Research Institute, Taiwan.

Work experience

2011 Teaching assistant, National Tsing Hua University, Taiwan.
2007 Math, English, and Nature Science in private school.

C. Peer-reviewed publications (in reverse chronological order).

1. Wu CC, Lien CC, **Hou WH**, Chiang PM, Tsai KJ. Gain of BDNF function in engrafted neural stem cells promotes the therapeutic potential for Alzheimer's disease. Sci Rep 2016, Accepted.

2. **Hou WH**, Kuo N, Fang GW, Huang HS, Wu KP, Zimmer A, Cheng JK, Lien CC. Wiring Specificity and Synaptic Diversity in the Mouse Lateral Central Amygdala. J Neurosci 2016 April; 36(16): 4549-4563.

3. Chang CP, Lee CT, **Hou WH**, Lin MS, Lai HL, Chien CL, Chang C, Cheng PL, Lien CC*, Chern Y. Type VI adenylyl cyclase negatively regulates GluN2B-mediated LTD and spatial reversal learning. Sci Rep 2016 Mar; 6(22529): 1-16.

D. Other publications

1. 連正章、**侯文賢**、王凱誼、高敏華。用光與化學分子控制大腦！《科學月刊（Science Monthly）》第 559 期/ 2016 年 7 月號 第 526-531 頁。